Astronomy & Astrophysics manuscript no. sn2011dh-2-aa-resubmit-v3
October 12, 2014

The Type IIb SN 2011dh - 2 years of observations and modelling of the lightcurves.

M. Ergon[1], A. Jerkstrand[2], J. Sollerman[1], N. Elias-Rosa[3], C. Fransson[1], M. Fraser[4,2], A. Pastorello[3], R. Kotak[2], S. Taubenberger[5], L. Tomasella[3], S. Valenti[6,7], S. Benetti[3], G. Helou[8], M.M. Kasliwal[9], J. Maund[2], S.J. Smartt[2], and J. Spyromilio[10]

[1] The Oskar Klein Centre, Department of Astronomy, AlbaNova, Stockholm University, 106 91 Stockholm, Sweden
[2] Astrophysics Research Centre, School of Mathematics and Physics, Queens University Belfast, Belfast, BT7 1NN, UK
[3] INAF, Osservatorio Astronomico di Padova, vicolo dell'Osservatorio n. 5, 35122 Padua, Italy
[4] Institute of Astronomy, University of Cambridge, Madingley Road, Cambridge, CB3 0HA
[5] Max-Planck-Institut für Astrophysik, Karl-Schwarzschild-Str. 1, D-85741 Garching, Germany
[6] Las Cumbres Observatory Global Telescope Network, 6740 Cortona Dr., Suite 102, Goleta, CA 93117, USA
[7] Department of Physics, University of California, Santa Barbara, Broida Hall, Mail Code 9530, Santa Barbara, CA 93106-9530, USA
[8] Infrared Processing and Analysis Center, California Institute of Technology, Pasadena, CA 91125, USA
[9] Observatories of the Carnegie Institution for Science, 813 Santa Barbara St, Pasadena, CA 91101, USA
[10] ESO, Karl-Schwarzschild-Strasse 2, 85748 Garching, Germany

Submitted to Astronomy and Astrophysics

ABSTRACT

We present optical and near-infrared (NIR) photometry and spectroscopy as well as modelling of the lightcurves of the Type IIb supernova (SN) 2011dh. Our extensive dataset, for which we here present the post 100 days observations, spans 2 years, and complemented with Spitzer mid-infrared (MIR) data, we use it to build a 3−732 days optical to MIR bolometric lightcurve. To model the <400 days bolometric lightcurve we use a hydrodynamical model grid, which allows us to determine the errors in the derived quantities, and a bolometric correction determined with steady-state NLTE modelling. Using this method we find a helium core mass of $3.1^{+0.7}_{-0.4}$ $M_{\odot}$ for SN 2011dh, consistent within error bars with previous results obtained using the <80 days bolometric lightcurve. We present 100−500 days bolometric and broad-band lightcurves for the Jerkstrand et al. (2014) steady-state NLTE models. The preferred 12 $M_{\odot}$ (initial mass) model, presented and found to give a good agreement with observed nebular spectra in Jerkstrand et al. (2014), shows a good overall agreement with the observed lightcurves, although some discrepancies exist. Time-dependent NLTE modelling shows that after ∼600 days a steady-state assumption is no longer valid. The radioactive energy deposition in this phase is likely dominated by the positrons emitted in the decay of ^{56}Co, but seems insufficient to reproduce the lightcurves, and what energy source is dominating the emitted flux is unclear. We find an excess in the *K* and the MIR bands developing between 100 and 250 days, during which an increase in the optical decline rate is also observed. A local origin of the excess is suggested by the depth of the He I 20581 Å absorption. Steady-state NLTE models with a modest dust opacity in the core (τ = 0.44), turned on during this period, reproduce the observed behaviour, but an additional excess in the Spitzer 4.5 μm band remains. CO first overtone band emission is detected at 206 days, and possibly at 89 days, and assuming the additional excess to be dominated by CO fundamental band emission, we find fundamental to first overtone band ratios considerably higher than observed in SN 1987A. The profiles of the [O I] 6300 Å and Mg I] 4571 Å lines show a remarkable similarity, suggesting these lines to originate mainly from the O/Ne/Mg zone, and using small scale fluctuations in the line profiles we estimate a filling factor of $\lesssim$0.07 for the emitting material. This paper concludes our extensive observational and modelling work on SN 2011dh. The results from hydrodynamical modelling, steady-state NLTE modelling and stellar evolutionary progenitor analysis are all consistent, and suggest an initial mass of ∼12 $M_{\odot}$ for the progenitor.

Key words. supernovae: general — supernovae: individual (SN 2011dh) — supernovae: individual (SN 1993J) — supernovae: individual (SN 2008ax) — galaxies: individual (M51)

1. Introduction

Type IIb supernovae (SNe) are observationally characterized by a transition from Type II (with hydrogen lines) at early times to Type Ib (without hydrogen lines but with helium lines) at later times. The physical interpretation is that these SNe arise from stars that have lost most of their hydrogen envelope, either through stellar winds or interaction with a binary companion. Which of these production channels dominates is still debated but for SN 1993J, the prime example of such a SN, a companion star was detected by direct observations (Maund et al. 2004; Fox et al. 2014). The evolution of this binary system has been successfully modelled (Podsiadlowski et al. 1993; Stancliffe & Eldridge 2009), and it is widely accepted that the companion was responsible for the removal of the hydrogen envelope. Bright, nearby Type IIb SNe as 1993J, 2008ax and the recent 2011dh are essential to improve our understanding of this class. Observations of the progenitor star in pre-explosion images, a search for the companion star when the SN has faded and multi-method modelling of high quality data, all provide important clues to the nature of Type IIb SNe and their progenitor stars.

In this paper we present the post 100 days part of our extensive optical and near-infrared (NIR) dataset, covering nearly two years, that we have obtained for SN 2011dh. The first 100 days of this dataset have been presented in Ergon et al. (2014a, hereafter E14a). Detailed hydrodynamical modelling of the SN using those data were presented in Bersten et al. (2012, hereafter B12) and steady-state NLTE modelling of nebular spectra in Jerkstrand et al. (2014, hereafter J14). Identification and analysis of the plausible progenitor star was presented in Maund et al. (2011, hereafter M11), and confirmation of the progenitor identification through its disappearance in E14a.

SN 2011dh was discovered on 2011 May 31.893 UT (Griga et al. 2011; Arcavi et al. 2011) in the nearby galaxy M51, and has been extensively monitored from X-ray to radio wavelengths. Most observations cover the 3−100 days period, but late-time data have been published by Tsvetkov et al. (2012), Van Dyk et al. (2013), Sahu et al. (2013), Shivvers et al. (2013) and Helou et al. (2013). As in E14a we focus on the ultra-violet (UV) to mid-infrared (MIR) emission. The explosion epoch (May 31.5 UT), the distance to M51 ($7.8^{+1.1}_{-0.9}$ Mpc) and the interstellar line-of-sight extinction towards the SN ($E(B\text{-}V)$=$0.07^{+0.07}_{-0.04}$ mag), are all adopted from E14a. The phase of the SN is expressed relative to this explosion epoch throughout the paper.

The nature of the progenitor star has been a key issue since the identification of a yellow supergiant in pre-explosion images, coincident with the SN (M11; Van Dyk et al. 2011). Recent progress in modelling of the SN (B12; J14; Shivvers et al. 2013), and the disappearance of the progenitor candidate (E14a; Van Dyk et al. 2013), strengthens the hypothesis that the progenitor was a yellow supergiant of moderate mass, as was originally proposed in M11. In this paper we present further modelling in support of this hypothesis. As shown in Benvenuto et al. (2013), a binary interaction scenario that reproduces the observed and modelled properties of the yellow supergiant is possible.

The paper is organized as follows. In Sect. 2 and 3 we present and analyse our photometric and spectroscopic observations, respectively, and compare these to SNe 1993J and 2008ax. In Sect. 4 we model the lightcurves and in Sect. **??** we discuss the MIR evolution, our results on the nature of the progenitor star, and the implication of these on our understanding of Type IIb SNe. Finally, we conclude and summarize our results in Sect. 6.

2. Photometry

Here we present observations spanning 100−732 days in the optical, 100−380 days in the NIR and 100−1061 days in the MIR, and provide analysis and comparisons with SNe 1993J and 2008ax. Hydrodynamical and steady-state NLTE modelling of these data are presented in Sect. 4. For SNe 1993J and 2008ax we adopt the same values and error bars for the distance and extinction as in E14a. The references for the photometric data of SNe 1993J and 2008ax used in the comparison are the same as specified in E14a. We note that the lack of S-corrected photometry for SN 1993J complicates the comparison, whereas for SN 2008ax, the S-corrected Johnson-Cousins (JC) photometry by Taubenberger et al. (2011) agrees reasonably well with the JC photometry by Tsvetkov et al. (2009).

2.1. Observations

The >100 days data were obtained with the Liverpool Telescope (LT), the Nordic Optical Telescope (NOT), Telescopio Nazionale (TNG), the Calar Alto 3.5m (CA 3.5m) and 2.2m (CA 2.2m) telescopes, the Asiago 67/92cm Schmidt (AS Schmidt) and 1.82m Copernico (AS 1.82m) telescopes, the William Herschel Telescope (WHT), the Albanova Telescope[1] (AT) and the United Kingdom Infrared Telescope (UKIRT). The late-time dataset includes 61 and 9 epochs of optical and NIR imaging, respectively, which gives a total of 146 and 32 epochs, respectively. Spitzer has systematically been observing SN 2011dh under program ID 70207 (PI Helou), 90240 and 10136 (PI Kasliwal). E14a and Helou et al. (2013) presented Spitzer photometry (using independent procedures) up to 85 and 625 days, respectively, and here we present observations up to 1061 days. Throughout the paper, we label the Spitzer 3.6 μm and 4.5 μm bands S_1 and S_2, respectively. The reduction and calibration procedures are described in detail in E14a, and issues specifically related to the >100 days data are discussed in Appendix A.

The S-corrected optical and NIR magnitudes and their corresponding errors are listed in Tables 4, 6, and 7 and the Spitzer magnitudes and their corresponding errors in Table 8. The magnitudes for the <800 days period, including the SWIFT magnitudes published in E14a and S-corrected magnitudes for the HST observations published in Van Dyk et al. (2013), are shown in Fig. 1. We also show cubic spline fits (E14a) or, when the sampling is sparse, linear interpolations, as well as extrapolations assuming a constant colour to adjacent bands. The extrapolation method used makes most sense in the early phase when the spectral energy distribution (SED) is dominated by the continuum. In particular, the NIR magnitudes are extrapolated between ~400 and ~750 days, which introduce a considerable uncertainty. Many calculations are based on these spline fits, interpolations and extrapolations, and the errors in the fitted splines have been taken as the standard deviation and then propagated.

2.2. Photometric evolution

In Fig. 2 we show absolute optical and NIR magnitudes for SNe 2011dh, 1993J and 2008ax, and in Table 1 we tabulate the tail decline rates at 100, 200 and 300 days. Most striking is the similarity between the lightcurves, except for a shift towards higher luminosities for SNe 1993J and 2008ax, the shift being larger in bluer bands and negligible in the NIR, and most pronounced for SN 2008ax. As discussed in E14a, this difference could be explained by errors in the adopted extinctions.

Given the caveat that SNe 1993J and 2008ax are only partly covered in U and NIR, we find the following general trends. At 100 days the V, R and I-band decline rates are roughly twice the decay rate of ^{56}Co, and subsequently decrease towards 300 days. The U and B-band decline rates are significantly lower at 100 days, subsequently approach the other optical decline rates and then evolve similarly. The J and H-band decline rates are considerably higher than the optical at 100 days, subsequently approaches those and eventually become considerably lower. For SNe 2011dh and 1993J, the K-band behaves quite differently than the other NIR bands. At 100 days the decline rate is significantly lower, but as it remains roughly constant, it subsequently approaches the other NIR decline rates and eventually becomes considerably higher. As seen in Fig. 1, the optical lightcurves of SN 2011dh flatten considerably after ~450 days, approaching a decline rate similar to, or lower than, the decay rate of ^{56}Co.

Both SNe 2011dh and 1993J were also monitored in the MIR, SN 2011dh in the S_1 and S_2 bands and SN 1993J in the

[1] 1.0 m Nasmyth-Cassegrain telescope at Albanova, Stockholm University. Equipped with an Andor DV438 CCD camera with an E2V 20C CCD chip and Bessel-like *UBVRI* filters.

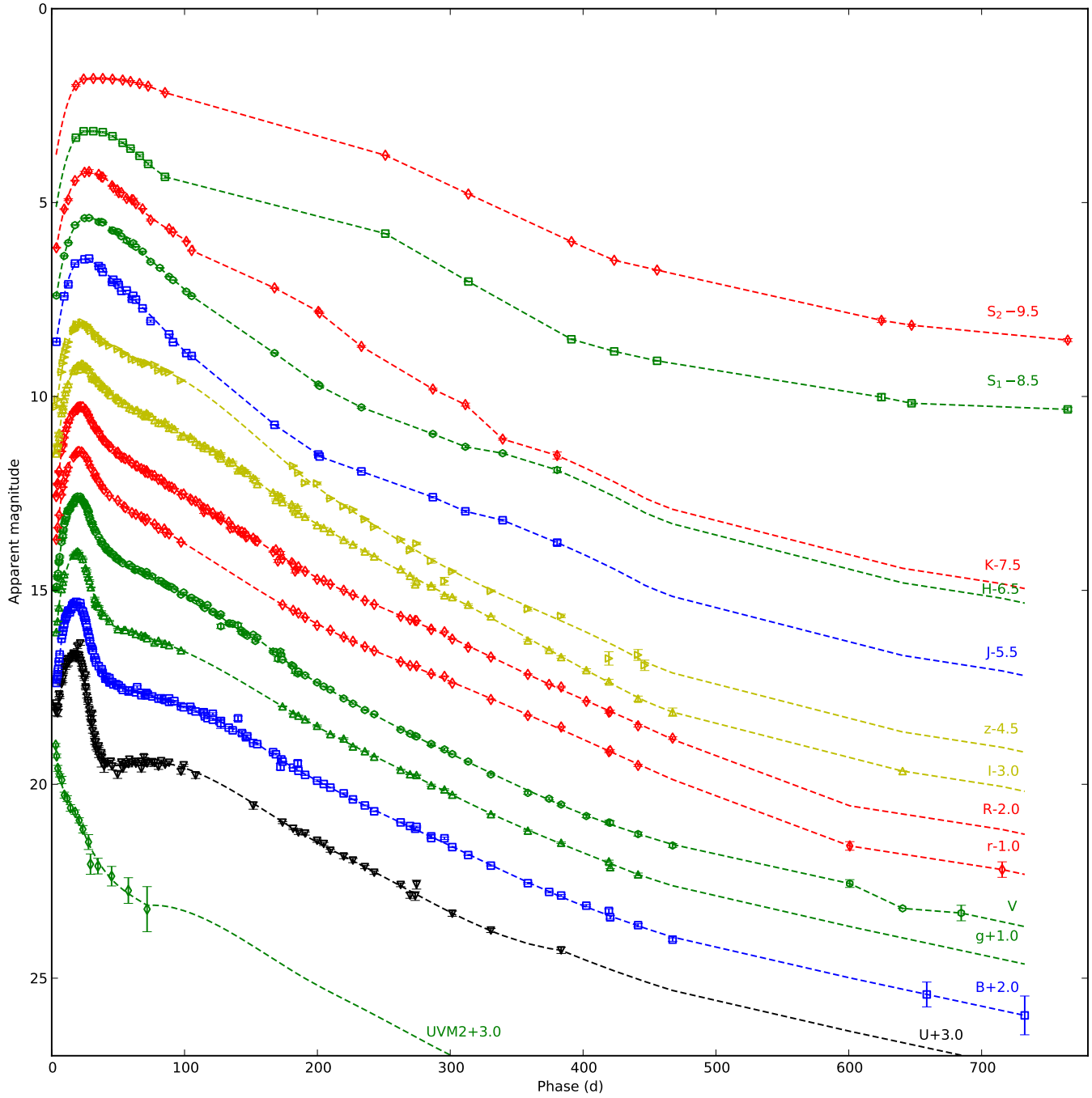

Fig. 1. Photometric evolution of SN 2011dh in the UV, optical, NIR and MIR. For clarity each band has been shifted in magnitude. Each lightcurve has been annotated with the name of the band and the shift applied. We also show combinations of spline fits, interpolations and extrapolations described in Sect 2.1 (dashed lines).

L band, which is similar to the S_1 band. For both SNe, a strong excess in the MIR develops between 100 and 250 days. For SN 1993J the MIR coverage ends at ∼250 days, and for SN 2011dh the subsequent evolution is fairly similar to the evolution in the optical. After ∼400 days, a considerable flattening of the MIR lightcurves is seen, similar to, but more pronounced than the flattening of the optical lightcurves. After ∼750 days (not shown in Fig. 1) this trend continues and the MIR lighcurves become almost flat.

2.3. Bolometric evolution

To calculate the bolometric lightcurves we use the spectroscopic and photometric methods described in E14a, applied to wavelength regions with and without spectral information, respectively. Combinations of spline fits, interpolations and extrapolations (Sect. 2.1; Figs. 1 and 2) have been used to calculate the magnitudes. Here and throughout the paper, the wavelength regions over which the luminosity is integrated are specified as follows; UV (1900−3300 Å), optical (3300−10000 Å), NIR (10000−24000 Å) and MIR (24000−50000 Å).

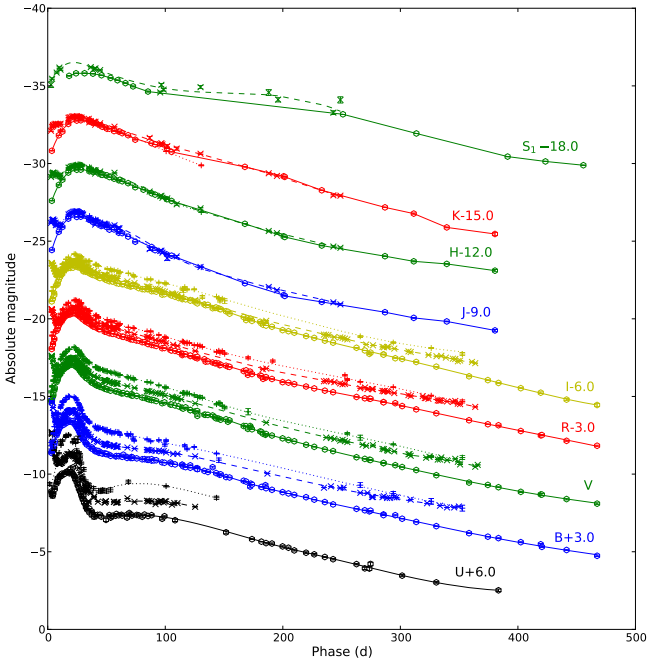

Fig. 2. Photometric evolution of SNe 2011dh (dots), 1993J (crosses) and 2008ax (pluses) in the optical and NIR. For clarity each band has been shifted in magnitude. Each lightcurve has been annotated with the name of the band and the shift applied. We also show combinations of spline fits, interpolations and extrapolations described in Sect. 2.1 (dashed lines).

Figure 3 shows the <500 days optical to NIR pseudo-bolometric lightcurves for SNe 2011dh, 1993J and 2008ax, as calculated with the photometric method, and in Table 1 we tabulate the decline rates at 100, 200 and 300 days. Given the caveat that SNe 1993J and 2008ax are not covered in NIR after ∼250 and ∼150 days, respectively, their optical to NIR pseudo-bolometric lightcurves are remarkably similar to the one of SN 2011dh, except for the shift towards higher luminosities mentioned in Sect. 2.2. The decline rates decrease from ∼0.020 mag day^{-1}, roughly twice the decay rate of ^{56}Co, at 100 days to ∼0.015 mag day^{-1} at 300 days. There is however a significant increase in the decline rate to ∼0.025 mag day^{-1} between 150 and 200 days for SN 2011dh, even more pronounced in the optical pseudo-bolometric lightcurve, not seen for SNe 1993J and 2008ax. For SN 1993J the decline rate becomes increasingly lower towards 300 days as compared to SNe 2011dh and 2008ax, which is consistent with an increasing contribution from circum-stellar medium (CSM) interaction in this phase.

Figure 4 shows the <750 days UV to MIR pseudo-bolometric lightcurve for SN 2011dh, as calculated with the combined spectroscopic and photometric methods, and in Table 10 we tabulate the 3−400 days period (for which we have full optical to MIR coverage) for reference. The decline rates are similar to those for the optical to NIR pseudo-bolometric lightcurve, but the increase between 150 and 200 days is not as pronounced. Given the caveats that the NIR coverage ends at ∼400 days, the UV to MIR pseudo-bolometric lightcurve shows a significant flattening after ∼400 days, and the decline rates for the 467-601 and 601-732 days periods are 0.0088 and 0.0061 mag day^{-1}, respectively. This flattening is also observed in the optical and MIR pseudo-bolometric lightcurves, for which we have full coverage, and after ∼750 days the MIR pseudo-bolometric lightcurve becomes almost flat. The optical decline rates are 0.0095 and 0.0069 mag day^{-1} for the 467−601 and 601−732 days periods, respectively, whereas the MIR decline rates are 0.0069, 0.0031 and 0.0006, for the 456−625, 625−765 and 765−1061 days periods, respectively. The flattening of the late-time lightcurves are discussed in more detail in Sect. 5.

Table 1. Broad-band and pseudo-bolometric decline rates at 100, 200 and 300 days for SN 2011dh, compared to SNe 1993J and 2008ax.

SN	Band	Rate (100 d) (mag day^{-1})	Rate (200 d) (mag day^{-1})	Rate (300 d) (mag day^{-1})
2011dh	*U*	0.011	0.019	0.017
2011dh	*B*	0.014	0.018	0.016
2011dh	*V*	0.019	0.021	0.017
2011dh	*R*	0.021	0.018	0.016
2011dh	*I*	0.019	0.020	0.018
2011dh	*J*	0.036	0.018	0.011
2011dh	*H*	0.029	0.019	0.011
2011dh	*K*	0.020	0.020	0.024
2011dh	*U*-*K*	0.021	0.019	0.016
1993J	*U*	0.006	...	...
1993J	*B*	0.011	0.017	0.012
1993J	*V*	0.019	0.018	0.017
1993J	*R*	0.022	0.014	0.013
1993J	*I*	0.022	0.018	0.013
1993J	*J*	0.041	0.017	...
1993J	*H*	0.033	0.018	...
1993J	*K*	0.022	0.024	...
1993J	*U*-*K*	0.021	0.017	0.013
2008ax	*U*	0.013	...	...
2008ax	*B*	0.015	0.018	0.016
2008ax	*V*	0.022	0.017	0.018
2008ax	*R*	0.023	0.015	0.016
2008ax	*I*	0.018	0.020	0.012
2008ax	*J*	0.035	...	...
2008ax	*H*	0.032	...	...
2008ax	*K*	0.032	...	...
2008ax	*U*-*K*	0.020	0.017	0.015

Figure 5 shows the fractional UV, optical, NIR and MIR luminosities for SN 2011dh. We assume the late-time extrapolated fractions to stay constant and do not use the adjacent colour based extrapolations applied elsewhere. At >100 days the most notable is the strong increase in the MIR fraction between 100 and 250 days, together with a simultaneous decrease in the optical fraction. Also notable is the increase in the NIR fraction between 200 and 400 days caused by the evolution in the *J* and *H* bands. The evolution becomes quite uncertain after ∼400 days when the NIR coverage ends, but there seems to be a continuous increase in the MIR fraction, at the expense of the optical fraction. Keeping the uncertainties in mind, it is worth noting the dominance of the optical luminosity even at ∼750 days.

Figure 6 shows the evolution of the SED as calculated with the photometric method, overplotted with blackbody fits to the *V*, *I*, *J*, *H* and *K* photometry as well as the observed (interpolated) spectra. At >100 days the most notable is again the strong excess developing in the MIR between 100 and 250 days. There is also a similar excess developing in the *K* band between 100 and 200 days, gradually fading away towards 300 days. The

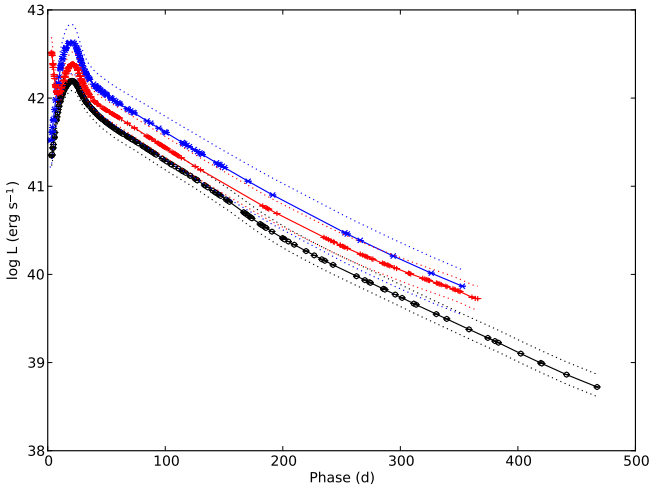

Fig. 3. Optical to NIR pseudo-bolometric lightcurve for SNe 2011dh (black circles and solid line), 1993J (red crosses and solid line) and 2008ax (blue pluses and solid line). The upper and lower error bars for the systematic error arising from extinction and distance (dotted lines) are also shown.

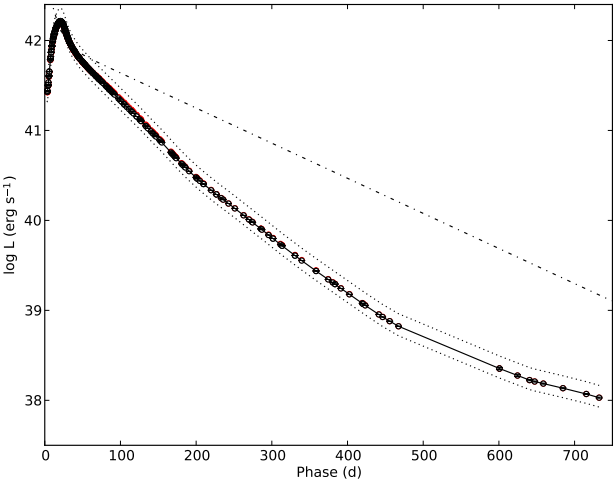

Fig. 4. UV to MIR pseudo-bolometric lightcurve for SN 2011dh (black circles and solid line). The upper and lower error bars for the systematic error arising from extinction and distance (black dotted lines) and the radioactive decay chain luminosity of 0.075 $M_\odot$ of ^{56}Ni (black dash-dotted line) are also shown.

evolution in the *K* and MIR bands, as well as the behaviour of the pseudo-bolometric lightcurves between 150 and 200 days, are discussed in more detail in Sect. 4.1.5, where we compare the observed lightcurves to results from modelling.

3. Spectroscopy

Here we present observations spanning 100−415 days in the optical and 100−206 days in the NIR, and provide analysis and comparisons with SNe 1993J and 2008ax. Steady-state NLTE modelling of these data, as well as a detailed analysis of the formation of the identified lines and the evolution of their fluxes, are presented in J14. Our analysis is complementary and focus mainly on the line profiles, and what can be learned about the distribution of the material from the different nuclear burning zones. Following J14 we subdivide the ejecta into a Fe/Co/He core surrounded by the Si/S zone, the oxygen-rich

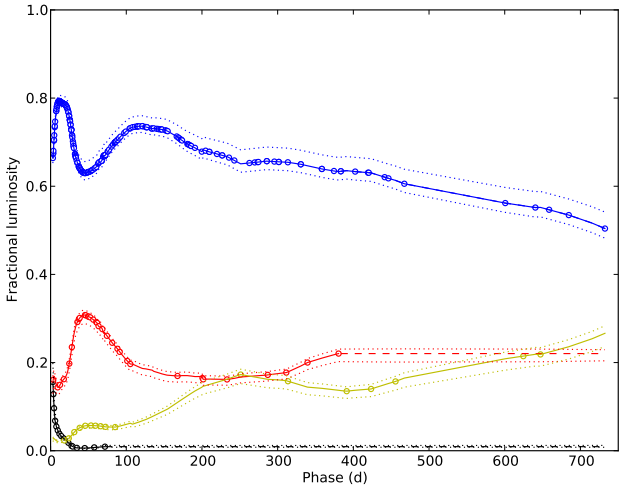

Fig. 5. Fractional UV (black dots), optical (blue dots), NIR (red dots) and MIR (yellow dots) luminosity for SN 2011dh. Interpolations and extrapolations are displayed as solid and dashed lines, respectively. The upper and lower error bars for the systematic error arising from extinction (dotted lines) are also shown.

O/Si/S, O/Ne/Mg and O/C zones, and the helium and hydrogen envelopes. This onion-line structure corresponds to what is obtained in 1-D modelling (e.g. Woosley & Heger 2007), whereas in multi-D modelling hydrodynamical instabilities results in macroscopic mixing of these zones (e.g. Iwamoto et al. 1997). We adopt a recession velocity of 515 km s^{-1} for SN 2011dh, as estimated from the Hα velocity map in Shetty et al. (2007). For SN 1993J and 2008ax we adopt the systematic recession velocities for M81 (−34 km s^{-1}; Tully et al. 2008) and NGC 4490 (565 km s^{-1}; Lavaux & Hudson 2011), respectively. The references for the spectroscopic data of SNe 1993J and 2008ax used in the comparison are the same as specified in E14a, but in addition we also include spectra for SN 2008ax from Milisavljevic et al. (2010), and unpublished spectra for SN 1993J obtained with the WHT and the Isaac Newton Telescope (INT) (P. Meikle et al.; private communication), described in J14.

3.1. Observations

The >100 days data were obtained with the NOT, the TNG, the WHT, the INT, the CA 2.2m, the AS 1.82m and the Gran Telescopio Canarias (GTC). Details of the late-time spectroscopic observations, the telescope and instrument used, epoch and instrument characteristics are given in Table 9. The late-time dataset includes 26 optical spectra obtained at 21 epochs and 2 NIR spectra obtained at 2 epochs, which gives a total of 81 optical spectra obtained at 47 epochs and 20 NIR spectra obtained at 12 epochs. The reductions and calibration procedures are described in detail in E14a.

All reduced, extracted and calibrated spectra will be made available for download from the Weizmann Interactive Supernova data REPository[2] (WISeREP) (Yaron & Gal-Yam 2012). Figure 7 shows the sequence of observed spectra, where those obtained on the same night using the same instrument have been combined. In addition to this, the 289, 292 and 293 days NOT spectra and the 228, 229, and 231 days INT spectra have been combined to increase the signal to noise ratio (SNR). For clarity some figures in this and the following sections are based on time-

[2] http://www.weizmann.ac.il/astrophysics/wiserep/

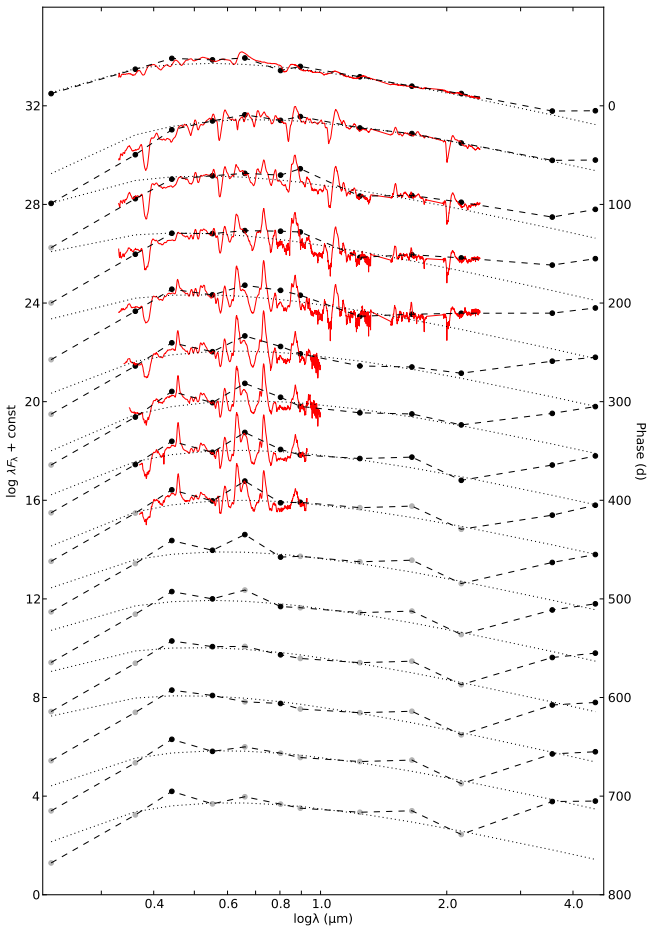

Fig. 6. The evolution of the SED as calculated with the photometric method (black dots and dashed lines) overplotted with blackbody fits to the V, I, J, H and K photometry (black dotted lines) as well as the observed spectra interpolated as described in Sect. 3.1 (red solid lines). Fluxes based on extrapolated magnitudes are displayed in shaded colour.

interpolations of the spectral sequence (E14a), and to further visualize the evolution the spectra have been aligned to a time axis at the right border of the panels. Interpolated spectra were used in the calculations of the bolometric lightcurve (Sect. 2.3) and S-corrections. Figure 8 shows the interpolated optical and NIR spectral evolution of SN 2011dh for 5−425 days with a 20-day sampling. All spectra in this and subsequent figures have been corrected for redshift and interstellar extinction.

3.2. Line evolution

Figure 9 shows the (interpolated) evolution for all the lines identified in J14, and most of these are also marked Fig. 8. Below we briefly discuss the evolution of the most important lines, and for a detailed discussion we refer to J14. As mentioned, the optical coverage ends at ∼400 days and the NIR coverage at ∼200 days.

There is an emerging emission feature near the rest wavelength of Hα, increasing in strength towards 450 days, but this feature is too narrow (∼5500 km s^{-1} as fitted with the line profile model described in Appendix B) to be consistent with the $\gtrsim$11000 km s^{-1} observed for the hydrogen envelope (E14a). As discussed in J14 this feature is rather due to [N II] 6548,6583 Å emission originating from the helium envelope. There is also a dip in the [O I] 6300,6364 Å line profile after ∼150 days (Fig. 11), that corresponds well to the early time Hα absorption minimum at ∼11000 km s^{-1} (E14a). However, as discussed in Sect. 3.6, this feature repeats in a number of other lines, and is rather due to clumping/asymmetries in the ejecta.

The prominent He I 10830 Å and He I 20581 Å lines show P-Cygni like profiles, extending in absorbtion to at least ∼10000 km $^{-1}$, and are still strong when the NIR coverage ends, whereas the He I 5016 Å line shows a P-Cygni like profile, extending in absorption to ∼5000 km s^{-1}, and fades away at ∼300 days. The He I 5876 Å line is likely scattered away in the Na I 5890,5896 Å line (J14), whereas the He I 6678 Å and He I 7065 Å lines are present at ∼100 days, but then quickly disappear.

The [O I] 6300,6364 Å line appears at ∼100 days, and grows to become the most prominent line at ∼400 days. The O I 7774 Å line shows a P-Cygni like profile until ∼300 days, extending in absorption to ∼8000 km s^{-1}, whereas the [O I] 5577 Å line fades away at ∼300 days. The O I 9263 Å line (blended with the Co II 9338,9344 Å line; J14) seems to be present at least until ∼400 days, whereas the O I 11290,11300 Å line is present until the NIR coverage ends. The Mg I] 4571 Å line appears at ∼150 days and increase in strength towards ∼400 days, whereas the Mg I 15040 Å line is present until the NIR coverage ends.

The Na I 5890,5896 line is present with a P-Cygni like profile until the optical coverage ends, extending in absorption to ∼10000 km s^{-1}. The Ca II 3934,3968 Å line shows a strong absorption profile, extending to ∼15000 km s^{-1}, and as the Ca II 8498,8542,8662 Å line it is present until the optical coverage ends. The latter shows an absorption component at ∼100 days, which quickly disappears, and the Ca II 8498,8542 Å contribution fades away towards ∼400 days. The [Ca II] 7291,7323 Å line appears at ∼100 days, soon becomes the most prominent line, and has a growing red wing extending to ∼10000 km s^{-1}, which could be caused by [Ni II] 7378,7411 Å emission (J14).

The [Fe II] 7155 Å line appears at ∼200 days in the blue wing of the [Ca II] 7291,7323 Å line and is present until the optical coverage ends. No other clear iron lines are present, but a distinct feature near 16450 Å , that could be either [Fe II] 16440 Å or [Si I] 16450 Å is present until the NIR coverage ends. The [Co II] 9338,9344 Å (blended with the O I 9263 Å line; J14) seems to be present at least until ∼300 days, whereas the [Co II] 10190,10248,10283 Å and [Co II] 15475 Å lines are present until the NIR coverage ends.

3.3. CO emission

The upper left panel of Fig. 10 shows the observed K-band spectrum at 206 days compared with the preferred steady-state NLTE model spectrum at 200 days, flux calibrated with the observed K-band flux at 206 days. The model (12F; see Sect. 4.1.2 and Appendix C.3) includes dust but not CO emission. The CO first overtone (Δv=2) emits between 2.25 and 2.45 μm and we have marked the location of the band heads, which are not sharp due to the Doppler broadening of the individual transitions contributing. There is a strong excess in this region as compared to the model spectrum, the integrated flux being 1.0×10^{-14} erg s^{-1} cm^{-2}. The contribution from this flux to the K-band flux is negligible though, due to the weak overlap with this band. We have used a simple LTE CO model described in Spyromilio et al. (1988) to provide a fit to the emission. The ratio of the band head emission is a diagnostic of the temperature of the CO, and

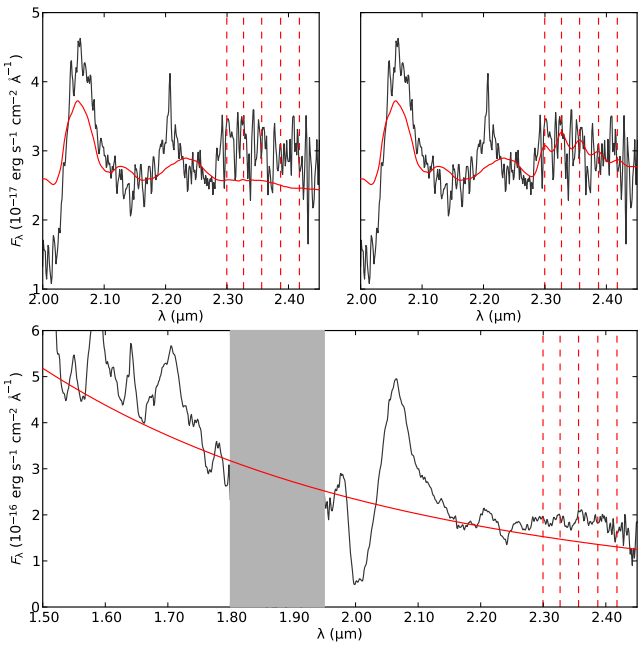

Fig. 10. Upper left panel: Observed (black solid line) and preferred steady-state NLTE model (red solid line) *K*-band spectra at 206 and 200 days, respectively. Upper right panel: The same, but with CO LTE model emission added to the steady-state NLTE model spectra. The CO overtone band heads have been marked by red dashed lines and the steady-state NLTE model spectra flux calibrated with the observed *K*-band flux at 206 days. Lower panel: Observed (black solid line) *H* and *K*-band spectrum at 89 days as compared to a blackbody fit to the continuum (red solid line).

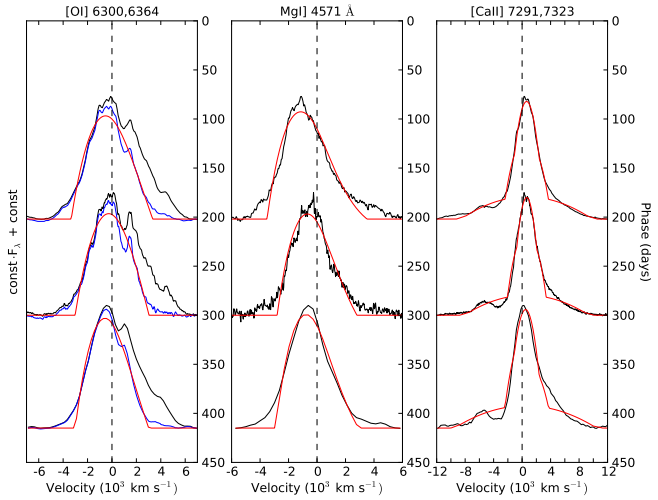

Fig. 11. [O I] 6300,6364 Å (left panel; black) and decomposed [O I] 6300 Å (left panel; blue), Mg I] 4571 Å (middle panel) and [Ca II] 7291,7323 Å line profiles (right panel) at selected epochs, as compared to line profile fits (red).

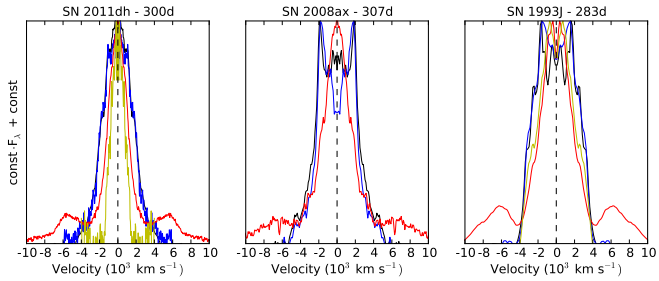

Fig. 12. Continuum subtracted mirrored blue-side profiles for the [O I] 6300,6364 Å (black), Mg I] 4571 Å (blue), [Ca II] 7291,7323 Å (red) and [Fe I] 7155 Å (yellow) lines for SNe 2011dh, 2008ax and 1993J at 300, 307 and 283 days respectively. The [Fe I] 7155 Å line is only shown for SN 2011dh.

the shape of the band heads a diagnostic of the expansion velocity of the CO gas. In the upper right panel of Fig. 10 we show the combined CO model and preferred steady-state NLTE model spectrum. The shape of the observed emission and the agreement with the simple CO model provides strong support for the identification of this feature with emission from the first overtone of CO. The temperature in the CO model is 2300 K and the emission region extends to 1500 km s^{-1}. The lower panel of Fig. 10 shows the observed *H* and *K*-band spectrum at 89 days. As this spectrum was obtained before 100 days, where the steady-state condition needed for the NLTE modelling is not satisfied, we instead use a blackbody fit to estimate the continuum. Although not as convincing as at 206 days, there is a clear excess in the region where we expect CO first overtone emission, the integrated flux being 7.2×10^{-14} erg s^{-1} cm^{-2}. The contribution from this flux to the *K*-band flux is again negligible. In the absence of a model for the underlying emission we have not tried to fit the excess emission with the LTE CO model, but the structure of the feature shows a reasonable agreement with the expected positions of the band heads.

3.4. Line emitting regions

The sizes of the line emitting regions are related to the distribution of the material from the different nuclear burning zones, determined by hydrodynamical instabilities in the explosion. In J14 we found the Mg I lines to arise from the O/Ne/Mg zone, the O I lines to arise from the O/Ne/Mg zone and, depending on the amount of molecular (CO and SiO) cooling, the O/C and O/Si/S zones. We also found the [Ca II] 7291,7323 Å line to arise mainly from the Si/S zone and the Fe II and Co II lines to arise from the Fe/Co/He zone. To measure the sizes of the line emitting regions, we fit a simple model for optically thin line emission to the observed line profiles. The model includes an absorptive continuum opacity to mimic blue-shifts caused by obscuration of receding side emission, and the details are given in Appendix B. The fits have been applied to lines for which the scattering contribution appears to be small, the SNR is good and contamination from other lines is likely to be small, and the results are given in Table 2. The estimated radii of the O I and Mg I line emitting regions of 2900−3400 and 2700−3600 km s^{-1}, respectively, are similar, whereas the estimated radii of the [Ca II] 7291,7323 Å and the Fe II and Co II line emitting regions of 2100−2500 and 1600−1800 km s^{-1}, respectively, are progressively smaller. This progression is consistent with the (unmixed) onion-like structure of the nuclear burning zones, and suggests incomplete mixing of the oxygen, Si/S and Fe/Co/He material. This is in agreement with results from multi-D hydrodynamical modelling, e.g. the 2-D hydrodynamical modelling of SN 1993J by Iwamoto et al. (1997), which shows significant differences in the distribution of the oxygen and Fe/Co/He material.

We have also compared the radii of the [O I] 6300 Å, Mg I] 4571 Å and [Ca II] 7291,7323 Å line emitting regions to those

Table 2. Sizes of the line emitting regions as measured from line profile fits. The fitted [Ca II] 7293/7323 Å and [Co II] 10190/10248, 10190/10283 Å line ratios are given in parenthesis.

Phase (d)	[O I] 6300,6364 Å (km s^{-1})	Mg I] 4571 Å (km s^{-1})	Mg I 15040 Å (km s^{-1})	[Ca II] 7293,7323 Å (km s^{-1})	[Fe II] 7155 Å (km s^{-1})	[Co II] 10190,10248,10283 Å (km s^{-1})
89	...	...	3500	...	...	1800 (0.44,0.02)
202	3400	3600	...	2400 (1.09)	...	...
206	...	...	3200	...	...	1800 (0.56,0.39)
300	3100	2800	...	2100 (1.05)	1600	...
415	2900	2700	...	2500 (0.39)	1700	...

of SNe 1993J and 2008ax. For SN 1993J the estimated radii are 4000−4100 and 3700−3900 km s^{-1} for the [O I] 6300 Å and Mg I] 4571 Å lines, respectively, and 3000−3400 km s^{-1} for the [Ca II] 7291,7323 Å line. For SN 2008ax the estimated radii are 3900−4000 and 3400−3600 km s^{-1} for the [O I] 6300 Å and Mg I] 4571 Å lines, respectively, and 2600−3000 km s^{-1} for the [Ca II] 7291,7323 Å line. These sizes are larger than those estimated for SN 2011dh, and larger for SN 1993J than for SN 2008ax. The radii of the Mg I] 4571 Å and the [O I] 6300 Å line emitting regions are again similar, and the radius of the [Ca II] 7291,7323 Å line emitting region is again smaller, suggesting incomplete mixing of the oxygen and Si/S material also for SNe 1993J and 2008ax. Figure 12 shows mirrored blue-side line profiles for the [O I] 6300 Å, Mg I] 4571 Å, [Ca II] 7291 Å and [Fe I] 7155 Å lines for SNe 1993J, 2008ax and 2011dh at ∼300 days. The blue side is less affected by obscuration as compared to the red side and contamination from the [O I] 6364 Å and [Ca II] 7323 Å lines to the [O I] 6300 Å and [Ca II] 7291 Å lines is probably modest. This figure nicely illustrates the different sizes of the line emitting regions discussed, and also shows a remarkable similarity of the blue-side [O I] 6300 Å and Mg I] 4571 Å line profiles for all SNe. For SN 2011dh this similarity persists also in small scale fluctuations (Sect. 3.6), which suggests these lines to arise mainly from the O/Ne/Mg zone, and the contributions from the O/C and O/Si/S zones to the [O I] 6300 Å flux to be modest.

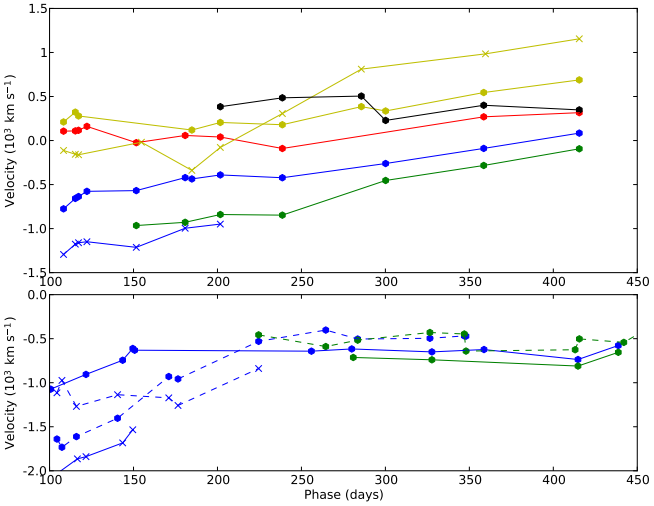

Fig. 13. Upper panel: Center of flux velocities for the [O I] 6300,6364 Å (blue circles), [O I] 5577 Å (blue pluses), Mg I] 4571 Å (green circles)), [Ca II] 7291,7323 Å (yellow circles), Ca II 8498,8542,8662 Å (yellow crosses), Na I 5890,5896 Å (red circles) and [Fe II] 7155 Å (black circles) lines for SN 2011dh. Lower panel: Center of flux velocities for the [O I] 6300,6364 Å (blue circles), [O I] 5577 Å (blue pluses) and Mg I] 4571 Å (green circles) lines for SNe 1993J (dashed lines) and 2008ax (solid lines).

3.5. Line asymmetries

Asymmetries in the line profiles may be caused by intrinsic asymmetries in the ejecta, radiative transfer effects, or blends with other lines. To measure the asymmetries we calculate the first wavelength moment of the flux (center of flux; Appendix B). The upper panel of Fig. 13 shows the evolution of the center of flux velocities for a selection of lines between 108 and 415 days for SN 2011dh. At early times the [O I] 6300,6364 Å, [O I] 5577 Å and Mg I] 4571 Å lines all show significant blue-shifts, which gradually disappear towards 400 days. As shown in the lower panel of Fig. 13, such blue-shifts are also present, and even more pronounced for SNe 1993J and 2008ax, but in this case the blue-shifts saturates at ∼500 km s^{-1} after 200 days. In J14 we provide a thorough discussion of these blue-shifts, and suggest the cause to be obscuration of receding-side emission by line-blocking in the core. We find no significant blue-shifts in the O I 11300 Å, O I 13164 Å and Mg I 15040 Å lines for SNe 2011dh and 2008ax in support of this hypothesis, as line-blocking is less effective in the NIR (J14). After ∼250 days we instead see increasing red-shifts in the [Ca II] 7291,7323 Å and Ca II 8498,8542,8662 Å lines for SN 2011dh which, given the findings in J14, are likely to be produced by blends with the [Ni II] 7378,7411 Å and [C I] 8727 Å lines, respectively. Given our interpretation of the line-shifts, the systematic redward trend seen in most lines between 250 and 400 days for SN 2011dh is coincidental.

Obscuration of receding-side emission may also be produced by dust in the ejecta, and as our steady-state NLTE models have a homogeneous dust opacity in the core (Sect. 4.1), in order to explain the behaviour of the lightcurves for SN 2011dh between 100 and 250 days (Sects. 2.3), it is not entirely clear how to disentangle the effects of line-blocking and dust. The version of the preferred model used in this work (12F) has an optical depth of 0.44, which is found to best reproduce the observed lightcurves, whereas the original version presented in J14 (12C) has an optical depth of 0.25. This lower value gives a worse reproduction of the lightcurves, but produce smaller blue-shifts, which seems to be in better agreement with observations. Using our line profile model and assuming a size of the line-emitting region of 3000 km s^{-1} (Sect. 3.4), we find blue-shifts of the center of flux of 150 and 250 km s^{-1} for optical depths of 0.25 and 0.44, respectively. At 415 days, when the effect from line-blocking would be the least, the center of flux for the [O I] 6300,6364 Å and Mg I]

4571 Å lines, which arise solely from the core (J14), shows a red-shift of ∼100 km s^{-1} and a blue-shift of ∼100 km s^{-1}, respectively. The absence of significant blue-shifts in these lines at 415 days suggests a small optical depth of the dust and indicate that, if the optical depth is as high as 0.44, the dust can not be homogeneously distributed within the core. It also suggests that the relatively large blue-shifts seen in these lines at earlier epochs can be attributed to the line-blocking effect.

3.6. Small scale fluctuations

Small scale fluctuations in the line profiles may provide evidence for a clumpy ejecta, as previously demonstrated for SNe 1987A (Stathakis et al. 1991; Chugai 1994) and 1993J (Spyromilio 1994; Matheson et al. 2000). In a simplified way we may represent the material of some nuclear burning zone by a number of randomly distributed clumps, having a typical size and occupying some fraction of the ejecta volume (filling factor). The small scale fluctuations then arise from statistical fluctuations in the distribution of the clumps, the RMS (Root Mean Square) of the fluctuations increasing with decreasing number of clumps or filling factor, or increasing size of the clumps.

Figure 14 shows small scale fluctuations in the [O I] 6300,6364 Å, [O I] 5577 Å, O I 7774 Å, Mg I] 4571 Å and Na I 5890,5896 Å lines at 202 and 300 days. The resolution is ∼600 and ∼250 km s^{-1} in the 202 and 300 days spectra, respectively, and the large scale (>1000 km s^{-1}) structure has been subtracted with the method described in Appendix B.4. In the upper left panel we show a comparison of the [O I] 6300 Å line at 202 and 300 days, and there is not much evolution in the small scale structure during this period. We identify 8 features marked A-H with a FWHM between 300 and 600 km s^{-1} present at both epochs. However, features G and H interpreted as belonging to the [O I] 6364 Å line, match very well with the E and F features interpreted as belonging to the [O I] 6300 Å line, so these are likely to be repetitions. Subtracting the [O I] 6364 Å flux using the method described in Appendix B.1, and minimizing the RMS of the small scale fluctuations redwards 3000 km s^{-1}, we find a line ratio of 2.9 at 202 and 300 days to give a complete removal of features G and H. This ratio is close to the 3.1 expected for optically thin emission and consistent with the results in J14.

In the upper right panel we show the decomposed [O I] 6300 Å line at 202 and 300 days, and in the lower left panel we show a comparison to the Mg I] 4571 Å line at 300 days. All features except B are clearly identified in both lines and the agreement is good. The features on the red side are weaker for the Mg I] 4571 Å line, which is consistent with the larger red-side flux deficit for this line (Fig. 11), but the relative (normalized with the large scale flux) strength of all features are similar. The good agreement suggests that the [O I] 6300 Å and Mg I] 4571 Å lines arise from the same nuclear burning zones. This, in turn, suggests that the Mg I] 4571 Å and [O I] 6300 Å lines arise mainly from the O/Ne/Mg zone, and that the contributions from the O/Si/S and O/C zones to the [O I] 6300 Å flux are modest (J14, Sect. 3.4).

In the lower right panel we show a comparison of the decomposed [O I] 6300 Å line and the [O I] 5577 Å, O I 7774 Å and Na I 5890,5896 Å lines at 202 days. The E and F features are clearly identified in all of these lines, whereas the other features are only seen in the [O I] 6300 Å line. Since the E and F features are also the strongest, it is not clear if the absence of the other features is real, or if they are just too faint to be seen. The small scale fluctuations in the [Ca II] 7291,7323 Å line (not shown) do not match

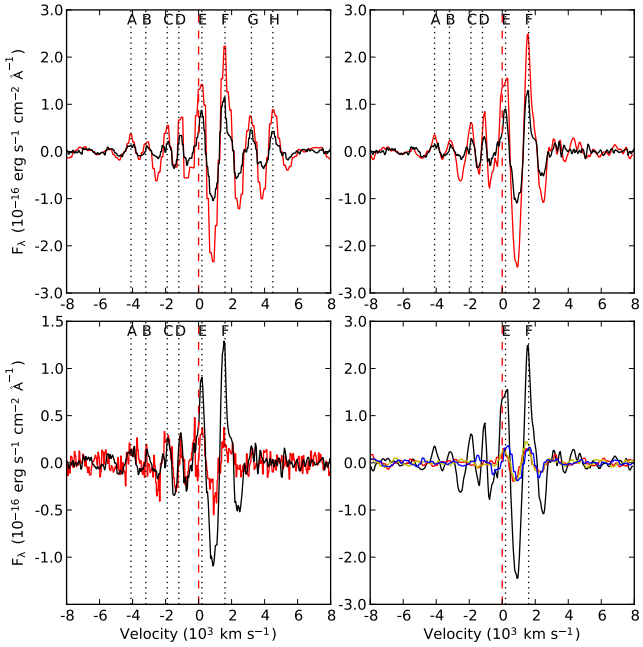

Fig. 14. Comparison of large scale subtracted line profiles. The upper left panel shows the [O I] 6300,6364 Å line at 202 (red) and 300 (black) days. The upper right panel shows the decomposed [O I] 6300 Å line at 202 (red) and 300 (black) days. The lower left panel shows the decomposed [O I] 6300 Å line (black) and the Mg I] 4571 Å line (red) at 300 days. The lower right panel shows the decomposed [O I] 6300 Å line (black) and the [O I] 5577 Å (red), O I 7774 Å (green) and Na I 5890,5896 Å (blue) lines at 202 days.

very well with those in the [O I] 6300 Å line, and the relative strength of the features is weaker. These results are consistent with the results in J14, where the oxygen lines are found to arise from the oxygen-rich zones and the Na I 5890,5896 Å line partly from the O/Ne/Mg zone, whereas the [Ca II] 7291,7323 Å line is found to arise mainly from other nuclear burning zones (Si/S).

Shivvers et al. (2013) presented an analysis of the [O I] 6300,6364 Å, O I 7774 Å and Mg I] 4571 Å lines at 268 days, where they by Gaussian decomposition find two narrow features, likely corresponding to our E and F features, repeating in all these lines, in agreement with our analysis. Matheson et al. (2000) presented an analysis of small scale fluctuations in the spectra of SN 1993J, and found a good agreement between the fluctuations in the [O I] 6300 Å, [O I] 5577 Å and O I 7774 Å lines, in agreement with our results for SN 2011dh. Surprisingly, they did not find a good agreement between the fluctuations in the [O I] 6300 Å and Mg I] 4571 Å lines. One possible explanation is that the [O I] 6300 Å line is dominated by flux from the O/Ne/Mg zone for SN 2011dh, but not for SN 1993J (see above). Filippenko & Sargent (1989) presented an analysis of small scale fluctuations in the spectra of the Type Ib SN 1985F. Similar to our analysis they found repetitions of the identified features in the [O I] 6300 Å and 6364 Å lines, and a line ratio close to 3 using the strongest feature.

Matheson et al. (2000) applied the statistical model by Chugai (1994) to their spectra of SN 1993J, giving a filling factor of ∼0.06 for oxygen zone material, distributed within a sphere with 3800 km s^{-1} radius. Using their estimated typical clump size of 300 km s^{-1}, this corresponds to ∼900 clumps. The model requires the radius of the sphere containing the clumps, the typ-

ical size of the clumps and the RMS of relative flux fluctuations in lines originating from the clumps. In the case of SN 2011dh, we adopt a radius of the sphere containing the bulk of the oxygen zone material of ∼3500 km s^{-1}, based on the estimates of the O I and Mg I line emitting regions in Sect. 3.2. For SN 1987A a typical clump size of 120 km s^{-1} was estimated from the power spectrum of the [O I] 6300 Å line by Stathakis et al. (1991), using high-resolution spectroscopy, but it is not clear how this was done by Matheson et al. (2000). As we do not have high-resolution spectroscopy for SN 2011dh, we can only estimate an upper limit on the typical clump size, taken to be 300 km s^{-1}, the smallest size of the features seen. The RMS of the relative flux fluctuations in the inner part (±2000 km s^{-1}, see Chugai 1994) of the sphere is ∼0.13 and ∼0.09 at 300 days for the decomposed [O I] 6300 Å line and the Mg I] 4571 Å line, respectively. Taking the latter value as a lower limit and applying Chugai (1994, eq. 11), we find an upper limit on the filling factor of oxygen zone material (within the sphere) of ∼0.07, and a lower limit on the number of oxygen zone clumps of ∼900. These values are similar to the values estimated by Matheson et al. (2000) for the clumping of oxygen zone material in SN 1993J.

4. Lightcurve modelling

Modelling of the SN lightcurves is usually restricted to bolometric lightcurves in the early phase, when the BC is small and the physics can be simplified. Except for 2003bg (Mazzali et al. 2009), we are not aware of any modelling of pseudo-bolometric or broad-band lightcurves for Type IIb or similar SNe at $\gtrsim$100 days, and it is therefore of great interest to examine this case using the high quality observations obtained for SN 2011dh. For this purpose we have constructed pseudo-bolometric and broad-band lightcurves for the set of spectral models presented in J14. These were calculated with the spectral synthesis code described in Jerkstrand et al. (2011, 2012), and as this code assumes steady-state, the models are limited to $\gtrsim$100 days, and due to the complexity of the physics involved, a restricted volume of parameter space is covered. Therefore, we also make use of HYDE, a hydrodynamical code described in Ergon et al. (2014b, herafter E14b) and summarized in Appendix D, which is limited to bolometric lightcurve modelling, but capable of evolving the SN through the explosion and diffusion phases, as well as scanning of large amounts of parameter space. Consistent modelling of the observed lightcurves from explosion to late times is not feasible, but combining the advantages of each code we are able to stretch the limitations. In Sect. 4.1 we present 100−500 days pseudo-bolometric and broad-band lightcurves for the J14 models, but also <100 days bolometric lightcurves for these models calculated with HYDE. In Sect. 4.2 we fit the <400 days optical to MIR pseudo-bolometric lightcurve to a grid of SN models calculated with HYDE, but only using a bolometric correction (BC) determined with the steady-state NLTE code this is possible.

4.1. Steady-state NLTE modelling of the 100−500 days pseudo-bolometric and broad-band lightcurves.

In J14 we present a set of spectral models for Type IIb SNe, with the specific aim to model SNe 1993J, 2008ax and, in particular, SN 2011dh. Here we present synthetic 100−500 days pseudo-bolometric and broad-band lightcurves for these models, constructed using the standard system filter response function specified in E14a. As mentioned, the J14 models cover a restricted volume of parameter space, which should be kept in mind. The preferred model for SN 2011dh, presented in J14, and refined in this paper with respect to dust, has been chosen to give the best agreement with both nebular spectra and the bolometric and broad-band lightcurves. In J14 we discuss the constraints on the model parameters provided by the nebular spectra, and here we discuss the constraints provided by the pseudo-bolometric and broad-band lightcurves. As mentioned, to investigate the behaviour of the models in the early phase, we also calculate <100 days bolometric lightcurves with HYDE. In this work we restrict the set of models (J14, table 3) to the model families differing in a single parameter (J14, table 4), and two additional models (12E and 12F) described in Appendix C.3. These models differ from model 12C only in the absence (12E) and the properties (12F) of the dust.

4.1.1. Model parameters

The models varies in the following parameters: initial mass (12, 13 or 17 M$_\odot$), macroscopic mixing (medium or strong), density contrast (low or high), positron trapping (local or non-local), molecular cooling (complete or none) and dust ($\tau_{\rm dust}$=0, 0.25 or 0.44). The initial mass, macroscopic mixing, contrast factor and positron trapping parameters are described in detail in J14, and we recommened reading sect. 3 in this paper. In short the initial mass parameter determines the overall properties of the ejecta model (e.g. mass, abundances and kinetic energy), whereas the macroscopic mixing and contrast factor parameters mimics the mixing of the nuclear burning zones and subsequent expansion of the Fe/Co/He clumps arising in mutli-D modelling. Note that the strong mixing models differs from the medium mixing models only in that 50 percent of the Fe/Co/He material is mixed into the helium envelope. The positron trapping parameter mimics the effect of a magnetic field (on the positron trapping), whereas the mass of ^{56}Ni is fixed at 0.075 M$_\odot$ (see Sect. 4.2).

The modelling does not include a self-consistent treatment of the formation of molecules and dust in the ejecta, but the effects of these are included in a simplified way as described in Appendices C.2 and C.3. The treatment of molecules includes only two extremes, no emission or complete dominance of the cooling in the O/C and O/Si/S zones by CO and SiO emission. This has some support in that molecules are efficient coolers and tend to dominate the cooling once formed, but is nevertheless simplified. Dust absorption is represented as a grey absorptive opacity in the core, and the emission as blackbody emission. Absorption is turned on at 200 days, and the optical depth chosen to reproduce the optical pseudo-bolometric lightcurve, whereas the temperature of the blackbody emission is determined from fits to the K and S_1 bands.

4.1.2. The preferred model.

The preferred model presented in J14 (12C) has an initial mass of 12 M$_\odot$, strong macroscopic mixing, local positron trapping, no molecular cooling, dust with $\tau_{\rm dust}$=0.25 and a high density contrast. However, in this work we use a refined version of the preferred model (12F), which differs only in the optical depth ($\tau_{\rm dust}$=0.44) and the temperature of the dust (Appendix C.3). The prefix "preferred" is used to distinguish from a best-fit model, as the one discussed in Sect. 4.2. It should be noted, that the good spectroscopic agreement found for model 12C in J14 does not necessarily apply to model 12F. However, for lines originating from the core, which are expected to be most affected by the higher optical depth of the dust, the flux would be ∼17 per-

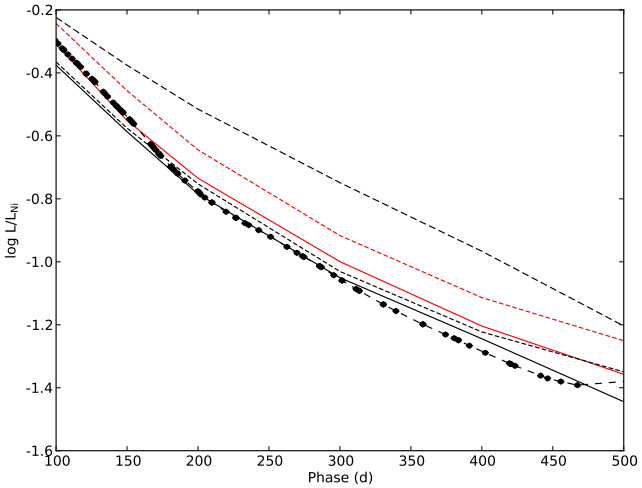

Fig. 15. The 100−500 days observed (black circles) and J14 model optical to MIR pseudo-bolometric lightcurves normalized to the radioactive decay chain luminosity of 0.075 $M_\odot$ of ^{56}Ni. Selected representatives (12A,12F,13A,13C,17A) of the model families differing in initial mass and macroscopic mixing are shown and displayed as follows: 12 $M_\odot$ (solid lines), 13 $M_\odot$ (short dashed lines), 17 $M_\odot$ (long dashed lines), medium mixing (red), strong mixing (black).

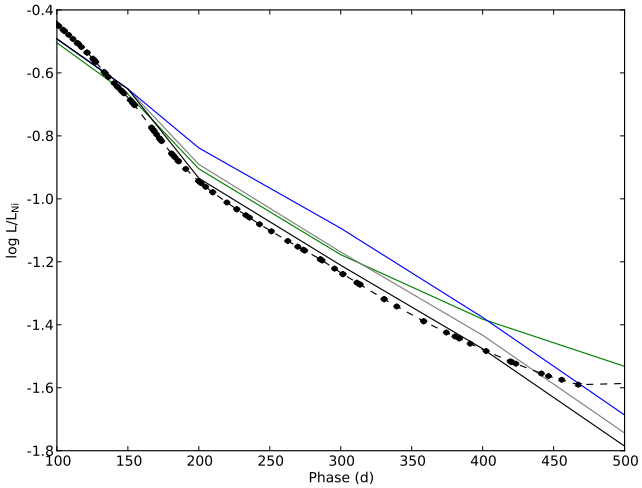

Fig. 16. The 100−500 days observed (black circles) and J14 model optical pseudo-bolometric lightcurves normalized to the radioactive decay chain luminosity of 0.075 $M_\odot$ of ^{56}Ni. The preferred model (12F; black solid line), model 12C (grey solid line) and model 12E (blue solid line), which differ only in the optical depth (12F; 0.44, 12C; 0.25, 12E; 0) and temperature of the dust, are shown together with model 12B (green solid line), which differs from model 12C only in the positron trapping (12C; local, 12B; non-local).

cent lower and the blue-shifts ∼100 km s^{-1} higher (Sect. 3.5), so the differences are likely to be small. Figures 15 and 16 show the 100−500 days preferred model and observed pseudo-bolometric lightcurves. In these figures, and a number of figures that follows, we have normalized the luminosity with the decay chain luminosity of the mass of ^{56}Ni, which (to first order) removes the dependence on this quantity. The preferred model shows a good agreement with observations, the differences being $\lesssim$10 and $\lesssim$15 percent for the optical and optical to MIR pseudo-bolometric lightcurves, respectively. However, after ∼400 days the observed optical pseudo-bolometric lightcurve flattens and starts to diverge from that of the preferred model. This flattening continues after 500 days and is discussed in Sect. 5. Figure 17 shows the preferred model and observed broad-band lightcurves. The preferred model shows an overall good agreement with observations, the differences being mostly $\lesssim$0.3 mag, but there are some notable exceptions, as the U and S_2 bands. The discrepancy seen in the optical pseudo-bolometric lightcurve after ∼400 days is also reflected in the B, g and V bands. The discrepancy in the S_2 band is discussed further in Sect. 4.1.5.

4.1.3. Calculation of the <100 days bolometric lightcurves with HYDE

Only after ∼100 days, steady-state is satisfied and the NLTE code can be used. Therefore we use HYDE in homologous mode to produce 3−100 days bolometric lightcurves for the J14 models. The J14 models are first (homologously) rescaled to day one, and then evolved with HYDE through the 1−100 days evolution. The initial temperature profile at 1 day is adopted from the best-fit hydrodynamical model for SN 2011dh (Sect. 4.2), with the mixing of the ^{56}Ni adjusted to match that of the J14 models. The subsequent evolution is not sensitive to the choice of initial temperature profile, as it is powered by the continuous injection of radioactive decay energy. Figure 18 shows the 3−100 days bolometric lightcurves for the J14 model families differing in initial mass and macroscopic mixing, as compared to the observed optical to MIR pseudo-bolometric lightcurve. The other steady-state

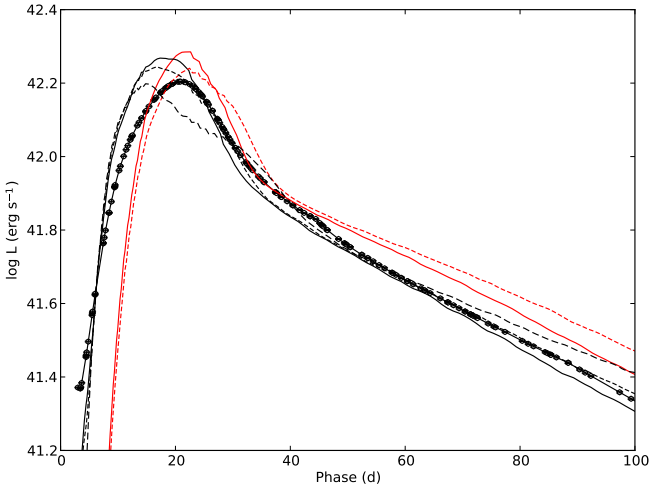

Fig. 18. The <100 days observed (black circles) and J14 model bolometric lightcurves as calculated with HYDE. The model families differing in initial mass and macroscopic mixing are shown and displayed as follows: 12 $M_\odot$ (solid lines), 13 $M_\odot$ (short dashed lines), 17 $M_\odot$ (long dashed lines), medium mixing (red), strong mixing (black).

NLTE model parameters have no or negligible influence on the bolometric lightcurve (Appendix C.1). The optical to MIR BC for the J14 models is likely >−0.15 mag during this period (Appendix C.1), so the comparison is justified. The preferred model shows an overall agreement with observations, although the peak occurs a few days earlier and is overproduced by ∼0.2 mag.

4.1.4. Constraints on the model parameters

As mentioned, the preferred model have been chosen to give the best agreement with both spectra and lightcurves, and here we discuss the constraints obtained from the lightcurves on the initial mass, macroscopic mixing, density contrast and positron

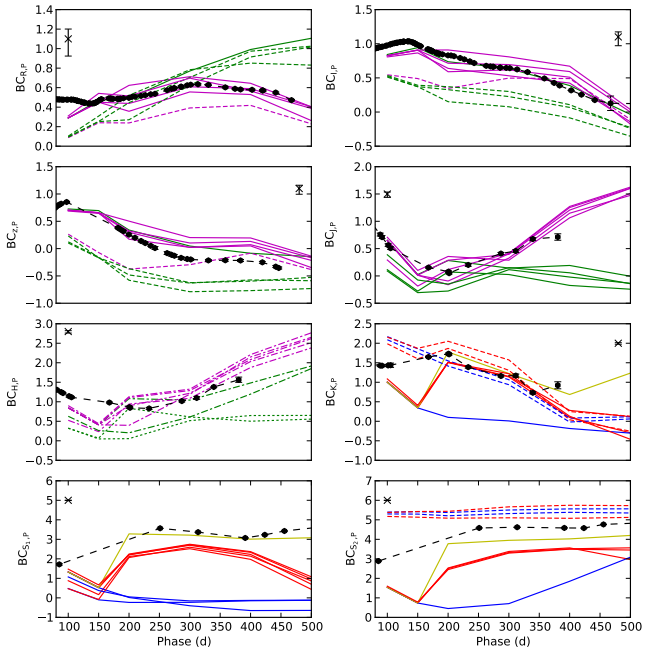

Fig. 19. The 100−500 days observed (black circles) and J14 model pseudo-BCs for selected bands and selected parameter families. The model parameter families are displayed as follows: complete molecular cooling (dashed lines), no molecular cooling (solid lines), high density contrast (dotted lines), low density contrast (dashed-dotted lines), local positron trapping (magenta), non-local positron trapping (green), $\tau_{\rm dust}$=0 (blue), $\tau_{\rm dust}$=0.25 (red), $\tau_{\rm dust}$=0.44 (yellow). 17 $M_\odot$ and medium mixing models are not displayed. To help reading the figures we display fitted magnitudes (Sect. 2.1) for well sampled bands. The error bars arising from the extinction is marked in the upper left or right corner.

trapping parameters. The constraints on the molecular cooling and dust parameters are discussed separately in Sect. 4.1.5. As explained in Appendix C.1 a factorisation of the lightcurves into bolometric lightcurves and BCs is useful for the analysis, as the bolometric lightcurve depends significantly only on the initial mass and macroscopic mixing, whereas the other parameters only significantly affects the BCs. Natural observational substitutes for these quantities are the optical to MIR pseudo-bolometric lightcurve and the pseudo-BCs, defined as described in Appendix C.1 and abbreviated as $BC_{X,P}$. For each parameter we have examined the effect on the model and observed UV to MIR pseudo-bolometric lightcurves, pseudo-BCs and broad-band photometry (which might provide strong constraints if the effects on the BCs and bolometric factors co-works), and compared with observation. Figure 19 shows the pseudo-BCs for those bands and parameter model families, for which useful constraints can be obtained.

Initial mass and macroscopic mixing Affects both the bolometric lightcurve and the BCs. The constraints from the optical to MIR pseudo-bolometric lightcurve are likely better obtained with the procedure used in Sect. 4.2. However, in agreement with the results obtained therein, 17 $M_\odot$ and medium mixing models seems to be excluded (Figs. 15 and 18). The effects on the BCs are generally too weak, or degenerate with the effects of other parameters, to provide useful constraints. On the other hand, *R*-band photometry seems to provide a constraint on the intial mass, even stronger than the one obtained from the bolometric lightcurve (Fig. 17). This is because the [O I] 6300,6364 Å line, which depends strongly on the initial mass (J14), contributes ∼50 percent of the flux in this band. Furthermore, as the fractional oxygen mass increase with initial mass (J14), both the *R*-band BC and the bolometric factor increase with initial mass, making *R*-band photometry particularly useful to constrain the initial mass. The choice of initial mass is motivated by the agreement with nebular spectra (J14) and the optical to MIR pseudo-bolometric and *R*-band lightcurves, whereas the choice of macroscopic mixing is motivated by the optical to MIR pseudo-bolometric lightcurve.

Density contrast Only significantly affects the BCs. In general the effect on the BCs is small, but there is a strong effect on BC_H at >300 days, caused by the [Si I] 16450 Å line. However, there is a degeneracy with a similar effect on BC_H, caused by the positron trapping (see below), and it is not possible to constrain the density contrast alone. Our NIR coverage ends at ∼400 days, but the observed evolution of $BC_{H,P}$ does not favour models with low density contrast and non-local positron trapping (Fig. 19). The choice of a high density contrast is mainly motivated by the agreement with nebular spectra (J14), and is also consistent with the upper limit on the oxygen zone filling factor of ∼0.07, derived from small scale fluctuations in the [O I] 6300,6364 Å and Mg I] 4571 Å lines (Sect. 3.6).

Positron trapping Only significantly affects the BCs. The effect is quite prominent at late times, when the positrons start to dominate the energy deposition, because locally trapped positrons deposit all their energy in the low temperature Fe/Co/He zone. This results in redder emission, and the luminosity of lines originating from this zone is boosted, whereas the luminosity of lines originating from other zones is reduced. Due to this, the optical BC decreases faster at >300 days for models with local trapping, which are in better agreement with the observed optical pseudo-bolometric lightcurve (Fig. 16). At >400 days, the observed optical decline rate starts to decrease, however, and models with local positron trapping start to diverge from observations. As discussed in Sect. 5, this could be a sign of additional energy sources, and is not necessarily in conflict with a scenario with locally trapped positrons. We find particularly strong line effects in BC_J and BC_H at >300 days, caused by the [Fe II] 12567 Å and [Fe II] 16440 Å lines, respectively. As discussed above, the effect on BC_H is degenerate with a similar effect caused by the density contrast. Our NIR coverage ends at ∼400 days, but the observed evolution of $BC_{J,P}$ seems to be in better agreement with models with local positron trapping (Fig. 19). The choice of local positron trapping is motivated by the optical pseudo-bolometric lightcurve and the evolution of $BC_{J,P}$ at 300−400 days, although the decreasing optical decline rate observed at >400 days is a caveat. The constraints obtained from nebular spectra are not conclusive (J14).

4.1.5. Dust, molecules and the MIR evolution

Perhaps the most interesting results obtained from the pseudo-bolometric and broad-band lightcurves are related to the MIR evolution and the molecular cooling and dust parameters, and therefore we discuss these separately. From Sect. 2 we know that there is a strong increase in the fractional MIR luminosity between 100 and 250 days, during which an increase in the decline rate of the optical pseudo-bolometric lightcurve is also

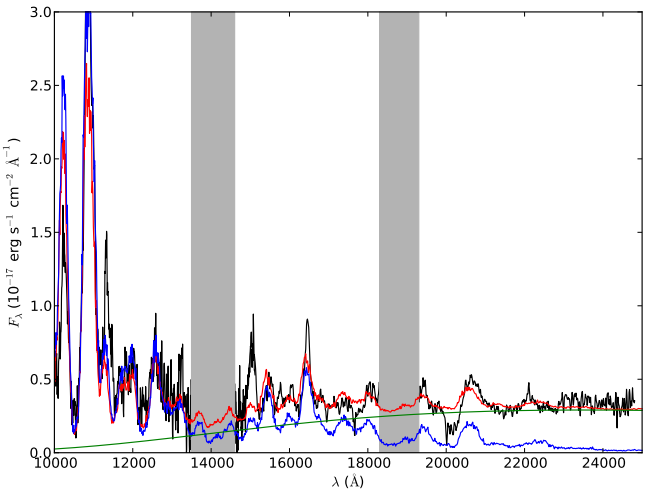

Fig. 20. Observed zJ and HK spectra at 198 and 206 days (black) compared to NIR spectra for the preferred model (12F; red) and model 12E (blue), which differs only in that $\tau_{\rm dust}$=0. The observed spectra were flux calibrated with the interpolated observed J, H and K magnitudes at 200 days and we also show the dust emission component for the preferred model (green).

observed. This behaviour is reminiscent of dust formation in the ejecta, and has previously been observed in SN 1987A (Suntzeff & Bouchet 1990). From E14a we know that there is an excess in the S_2 band, as compared to blackbody fits, developing already during the first hundred days. The S_2 band overlaps with both the CO fundamental band and the SiO first overtone band, so in this band molecule emission provides an alternative or complementary explanation. We also know from Sect. 3.3 that some amount of CO first overtone emission is observed at 206 days, and possibly at 89 days, which implies at least some contribution from CO fundamental band emission to the S_2 flux. Below we discuss the constraints obtained from the lightcurves, but also additional constraints obtained from spectra not discussed in J14.

dust Only affects the BCs and tends to decrease the optical emission and increase the K-band and MIR emission, as the hot radiation from the SN is absorbed and re-emitted at a much lower temperature. CO first overtone emission contributes negligible to the K band flux (Sect. 3.3), so the observed excess in this band can be solely attributed to dust emission. As mentioned, models with dust has a dust opacity in the core, turned on at 200 days, which results in a decrease of the optical BC and a simultaneous increase of $\rm BC_{\it K}$ and the MIR BCs. The preferred model (with $\tau_{\rm dust}$=0.44) well reproduces both the drop in the optical pseudo-bolometric lightcurve (Fig. 16) and the increase in $\rm BC_{\it K,P}$ and $\rm BC_{\it S_1,P}$ (Fig. 19), whereas the original J14 models (with $\tau_{\rm dust}$=0.25) only qualitatively reproduce this behaviour. This shows, most importantly, that the absorbed and emitted luminosities are in good agreement, and suggests a scenario where the emission arise from nearby, newly formed dust, presumably in the ejecta. Note that the dust contribution is insufficient to reproduce the excess in S_2 band (Fig. 19), suggesting a contribution from molecule emission in this band (see below). Further support for a local origin of the emission is gained from spectra. In Fig. 20 we show the observed NIR spectrum at ∼200 days, as compared to NIR spectra for the preferred model and model 12E (without dust) at 200 days, as well as the dust emission component for the preferred model. The observed flux at the absorption minimum of the He I 20581 Å line is a factor of ∼2 below the model dust emission level[3], which suggests this emission to originate from $\lesssim$10000 km s^{-1}, and disfavours a thermal echo from heated CSM dust (but see Helou et al. 2013). Regardless of the location, dust emission seems to be required to explain the strong discrepancy between observations and models without dust in the K and S_1 bands (Fig. 19), further supported by the spectral comparison in Fig. 20. The small blue-shifts in the [O I] 6300,6364 Å and Mg I] 4571 Å lines at 415 days (Sect. 3.5) and the lack of a physical model for the temperature evolution are caveats though. A MIR excess developing between 100 and 250 days was also observed for SN 1993J (Sect. 2.3). The cause of this excess was suggested by Matthews et al. (2002) to be dust, but the absence of an increase in the optical pseudo-bolometric decline rate indicates that, if this emission is due to dust, it would rather arise from heated CSM dust. Except for SNe 2011dh and 1993J, we have found no reports of dust emission in Type IIb or stripped envelope SNe in the literature.

molecular cooling Only affects the BCs and results in a redistribution of cooling emission from the O/C and O/Si/S zones to the CO and SiO molecular bands. The effect is strong in the S_2 band, which overlaps with the CO fundamental and SiO first overtone bands, and there is also a significant effect in the K band, which overlaps partly with the CO first overtone band. The observed CO first overtone emission implies some amount of CO cooling in the O/C zone at 206 days, and possibly at 89 days, but is ∼2.5 and ∼3.5 mag too faint, respectively, as compared to models with complete molecular cooling. As compared to models with complete molecular cooling (with or without dust), the observed $\rm BC_{\it S_2,P}$ is ∼2 and 0.5−1.0 mag too small at 85 and >251 days (Fig. 19). On the other hand, as compared to the preferred model (without molecular cooling, but with dust), which shows the best agreement in the K and S_1 bands for a conceivable dust component (see above), the observed $\rm BC_{\it S_2,P}$ is 0.5−1.0 mag too large (Fig. 19). As molecule emission in the S_2 band is likely to be dominated by the CO fundamental band (Appendix C.2), this suggests a small amount of CO cooling in the O/C zone at 85 days, increasing to an intermediate amount at >251 days, whereas the observed CO first overtone emission suggests a small amount of molecular cooling at 89 and 206 days.

The interpretation of the CO first overtone emission and the S_2 excess depends on the fundamental to first overtone band ratio, which is assumed to be the same as observed in SN 1987A (Appendix C.2). The observed CO first overtone and S_2 fluxes give an upper limit on this ratio, which can be improved by subtracting a model for the underlying emission, and if we again assume the excess in the S_2 band to be dominated by CO fundamental band emission, we can estimate it. Using the preferred model for the underlying emission, keeping in mind that the S_2 magnitudes have to be interpolated between 85 and 251 days, we get upper limits of 6.8 and 16 and estimates of 4.5 and 7.7 at 89 and 206 days, respectively. These values are significantly larger than in the models (∼1 and ∼2, respectively), and would naively suggest a lower temperature for the CO. So, either the fundamental to first overtone band ratios are significantly higher than observed in SN 1987A or the excess in the S_2 band is not caused by CO (but e.g. SiO or heated CSM dust).

[3] Note that the model dust emission has not been subject to radiative transfer (Appendix C.3), so the depth of the model He I 20581 Å absorption corresponds to that expected for a thermal echo.

Further constraints on the amount of molecular cooling is gained from thermal lines originating in the O/C an O/Si/S zones, in particular the blended Ca II 8498,8542,8662 Å and [C I] 8727 Å lines (J14). The evolution of this blend is reflected in the evolution of the I and z bands, which seems to exclude models with complete molecular cooling at $\lesssim$250 days (Fig. 19; but see also J14), and likely also at later times due to continued presence of the [C I] 8727 Å line (Sect. 3.2). Finally, the remarkable similarity between the [O I] 6300 Å and Mg I] 4571 Å line profiles, suggests the contributions to the [O I] 6300 Å flux from the O/C and O/Si/S zones to be modest (Sect. 3.4), in turn suggesting a considerable amount of molecular cooling at $\gtrsim$200 days. Although the constraints are not conclusive, they are not necessarily inconsistent, and at least in the O/C zone, a scenario with a small of amount of molecular (CO) cooling at ~100 days, increasing to an intermediate amount at $\gtrsim$250 days, seems reasonable. CO emission has been reported for the Type Ic SNe 2002ew (Gerardy et al. 2002) and 2007gr (Hunter et al. 2009), but for Type Ib and IIb SNe we have found no reports of CO emission in the literature. There is a feature near 23000 Å however, in the NIR spectra of SN 1993J (Matthews et al. 2002), that could be interpreted as a modest amount of CO first overtone emission.

4.2. Hydrodynamical modelling of the <400 days optical to MIR pseudo-bolometric lightcurve

B12 presented hydrodynamical modelling of SN 2011dh, that well reproduced the <80 days UV to MIR pseudo-bolometric lightcurve presented in E14a. In E14b we use a grid of SN models constructed with HYDE and MESA STAR (Paxton et al. 2011, 2013), to fit the <100 days UV to MIR bolometric lightcurve, and here we use an extended version of this model grid to fit the <400 days optical to MIR pseudo-bolometric lightcurve. This is the period for which we have full U to S_2 coverage and, except for the additional ~300 days of data, the method allows us to quantify the errors in the derived quantities and the degeneracy of the solution, issues discussed in E14a from approximate considerations. The stellar models consists of bare helium cores without a hydrogen envelope, which is a sound approximation as long as the optical depth of the hydrogen envelope is $\ll$1, and the mass low enough not to (appreciable) decelerate the helium core (E14b). The original model grid is described in E14b and the extended one summarized in Appendix D, and the model parameters are the helium core mass (M_{He}), the explosion energy (E), and the mass (M_{Ni}) and distribution (Mix_{Ni}) of the ^{56}Ni. At <100 days the optical to MIR BC is likely >−0.15 mag (Appendix C.1) and is assumed to be negligible, but at >100 days knowledge of the optical to MIR BC is essential, and here we take advantage of results obtained with the steady-state NLTE code as described below. The fitting is done by minimization of the square of the relative residuals, giving equal weights to the diffusion phase lightcurve, the early tail lightcurve, the late tail lightcurve and the diffusion phase photospheric velocities.

Bolometric correction To determine how the BC varies in the parameter space of the hydrodynamical model grid is not computationally feasible. Instead, we take advantage of the fact that the BC varies with <±0.1 mag between the J14 steady-state NLTE models during the 100−400 days period (Appendix C.1), and use the BC for the preferred steady-state NLTE model for all hydrodynamical models. However, as the J14 models cover a restricted volume of the hydrodynamical parameter space, we need to justify this choice further. It is reasonable to assume that the BC depends mainly on the energy deposition per unit mass (determining the heating rate) and the density (determining the cooling rate). Furthermore, we know beforehand, that models giving a bad <100 days fit will not give a good <400 days fit. Inspecting the J14 models and the hydrodynamical models with a normalized standard deviation in the <100 days fit less than 3, we find that these hydrodynamical models do not span a wide range in (mass averaged) density or energy deposition per mass, and that the J14 models cover about half of this region. Although these quantities evolve quite strongly with time, they scale in a similar way for all models, and this conclusion holds for the full 100−400 days period. The effect of not varying the steady-state NLTE parameters that do not map onto the hydrodynamical parameter space (dust, molecular cooling, positron trapping and density contrast) is harder to constrain. The small spread in the BC for the J14 models during the 100−400 days period, make this caveat less worrying though.

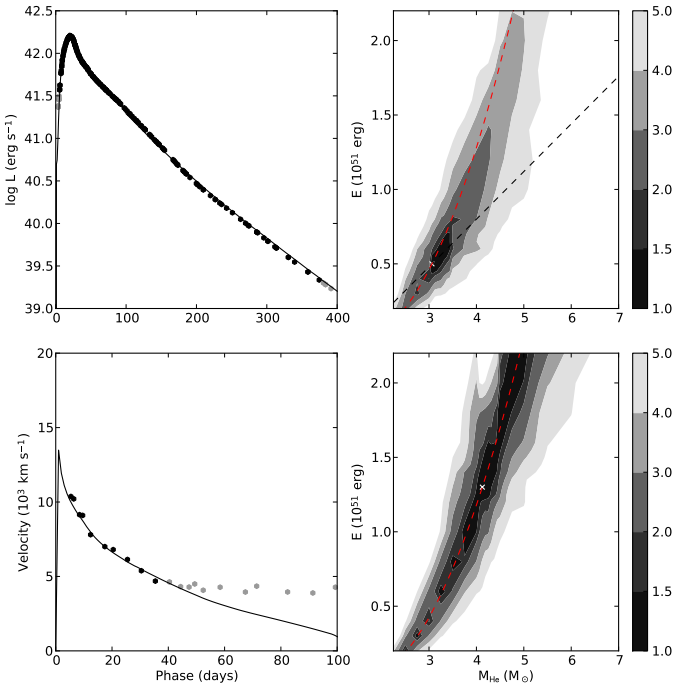

Fig. 21. Left panels: Optical to MIR pseudo-bolometric lightcurve (upper left panel) and photospheric velocities (lower left panel) for the best-fit model as compared to the observed optical to MIR pseudo-bolometric lightcurve and velocities for the absorption minimum of the Fe II 5169 Å line for SN 2011dh. Observations not included in the fit are displayed in grey. Right panels: Contour plots showing the (grey-scale coded) standard deviation in the fit, normalized to that of the best-fit model, projected onto the E-M_{He} plane for the case where the photospheric velocities were used (upper right panel) and not used (lower right panel). We also show the constraints M_{ej}/E=const (blue) and M_{ej}^2/E=const (red) provided by the photospheric velocities and the bolometric lightcurve, respectively (E14b).

Results The left panels of Fig. 21 show the best-fit model optical to MIR pseudo-bolometric lightcurve and photospheric velocities, as compared to the observed optical to MIR pseudo-bolometric lightcurve and velocities for the absorption minimum of the Fe II 5169 Å line. The upper an lower right panels of

Table 3. Helium core mass, explosion energy and mass and distribution of the ^{56}Ni as derived from the <400 days optical to MIR lightcurve in this work, and from the <80 and <100 days UV to MIR pseudo-bolometric lightcurves in B12 and E14b, respectively.

Reference	M_{He} ($M_\odot$)	E (erg)	M_{Ni} ($M_\odot$)	Mix_{Ni}
This work	3.06 (+0.68,-0.44)	0.50 (+0.42,-0.22)	0.075 (+0.028,-0.020)	0.95 (+0.06,-0.04)
E14b	3.31 (+0.54,-0.57)	0.55 (+0.35,-0.28)	0.075 (+0.028,-0.020)	1.05 (+0.08,-0.00)
B12	3.3-4.0	0.6-1.0	0.06-0.10	0.95

Fig. 21 show contour plots of the standard deviation in the fit, normalized to that of the best-fit model, for the case when the fitting was done using both the lightcurve and the photospheric velocities and the lightcurve alone, respectively. The fits to the lightcurve and the photospheric velocities are both good, and when the photospheric velocities are used the solution is well constrained in the E-M_{He} plane. When the fit is done using the lightcurve alone the solution is completely degenerate along the M_{ej}^2/E=const curve, in agreement with the results for <100 days lighcurves discussed in E14b. The good fit to the lightcurve suggests that other isotopes than ^{56}Ni and ^{56}Co, or additional energy sources like those discussed in Sect. 5, do not contribute substantially to the luminosity before 400 days. Table 3 lists the best-fit values for the helium core mass, explosion energy and mass and distribution of the ^{56}Ni, as well as the results obtained in B12 and E14b, and the results for the <400 days lightcurve are consistent within error bars with those for the <80 and <100 days lightcurves obtained in B12 and E14b. The addition of the late-time data seems to decrease the explosion energy and helium core mass slightly, and these are ∼10 percent lower as compared to the results obtained in E14b. The strong mixing of the ^{56}Ni found (95 percent in mass, see Appendix D), is in good agreement with the results obtained in B12 and E14b, and seems to be required to fit the rise to peak luminosity (see also Sect. 4.1.4). The fraction of the ^{56}Ni outside 3500 km $^{-1}$ is ∼50 percent in the best-fit model, and naively this is in contradiction with the small size of the Fe/Co/He line emitting region estimated in Sect. 3.2. However, the amount of high velocity Fe/Co/He material does not necessarily need to be high to reproduce the rise to peak luminosity, and further modelling is needed to resolve this issue. The errors in the derived quantities are propagated from the errors in the observed quantities (distance, extinction and a systematic error of 15 percent in the photospheric velocities), but does not take into account the degeneracy of the solution. However, as is evident from the contour plots, the constraint on the quantity M_{ej}^2/E is strong, and even if the photospheric velocities were considerably *underestimated*, which seem unlikely, a helium core mass of $\gtrsim$4 $M_\odot$ would be excluded.

5. The >500 days lightcurves

As discussed in Sects.2.3 there is a strong flattening of the observed pseudo-bolometric lightcurves after ∼450 days[4], which is also when these start to diverge from the preferred steady-state NLTE model (Sect. 4.1.2). Figure 22 shows the >200 days observed optical to MIR, optical plus MIR (excluding NIR), optical and MIR pseudo-bolometric lightcurves, as compared to the bolometric lightcurve, deposited ^{56}Co γ-ray and positron luminosity and deposited ^{57}Co luminosity for the preferred steady-state NLTE model[5]. As is clear from the figure, the deposited ^{56}Co luminosity is dominated by the positron contribution after ∼450 days, and the observed $\gtrsim$600 days lightcurves are unlikely to be powered by the γ-rays emitted in the ^{56}Co decay. Shivvers et al. (2013) suggested that the SN has entered a phase powered by the positrons emitted in the ^{56}Co decay after 300−350 days. Given our results, this suggestion seems to be roughly correct in the sense that the positron contribution dominates the deposited luminosity after ∼450 days. However, as we discuss below, there is evidence for additional energy sources and the positron contribution does not seem to dominate the emitted luminosity.

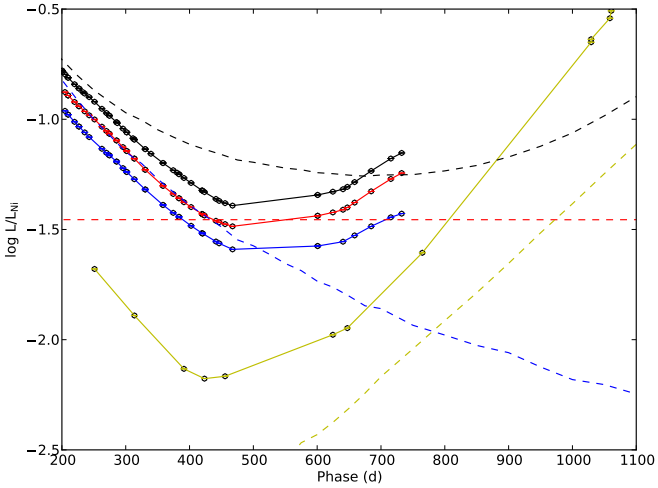

Fig. 22. The >200 days optical to MIR (black dots), optical plus MIR (red dots), optical (blue dots) and MIR (yellow dots) pseudo-bolometric lightcurves, as compared to the bolometric lightcurve (black dashed line), deposited ^{56}Co γ-ray (blue dashed line) and positron (red dashed line) luminosity and deposited ^{57}Co luminosity (yellow dashed line) for the preferred steady-state NLTE model (12F). The lightcurves have been normalized to the radioactive decay chain luminosity of 0.075 $M_\odot$ of ^{56}Ni.

The J14 models were not evolved beyond 500 days as the steady-state condition is no longer valid (see below). However, a similar set of models, which were evolved to 700 days, all show a decrease in the optical and optical to MIR BCs after 500 days, corresponding to redder emission. This decrease is particularly strong for models with local positron trapping due to the increasing contribution from the low temperature Fe/Co/He zone. Assuming that the actual BCs behave similary and do not increase, the $\gtrsim$600 days pseudo-bolometric decline rates, which becomes significantly lower than the decay rate of ^{56}Co (Sect. 2.3), are not consistent with a model powered by this decay. Furthemore, assuming again that the actual BCs do not increase, the actual

[4] Note that there is observational gap between 467 and 601 days.

[5] These were calculated with HYDE using the same ejecta model as the preferred steady-state NLTE model.

bolometric luminosity at 732 days would be $\gtrsim$0.6 mag higher than the radioactive energy deposition in the preferred model. Even if we ignore the BCs, the observed optical plus MIR luminosity at 732 days equals the radioactive energy deposition in the preferred model, and the observed MIR luminosity at 1060 days is 1.1 mag higher. So both the observed decline rates and the observed luminosities suggest that additional energy sources are required to power the $\gtrsim$600 days lightcurves.

If the recombination time scales become longer than the time scale of the ^{56}Co decay, some fraction of the energy is deposited in a growing inoziation reservoir, which through recombination emission could eventually dominate the emitted luminosity. This process, called freeze-out, is an example of time-dependent effects that might violate the steady-state assumption in late phases. We use a time-dependent NLTE code (Kozma & Fransson 1992, 1998a,b) to test this assumption, and find that time-dependent effects start to become important at ~600 days, and after ~800 days they provide a dominant and increasing contribution to the optical flux. In the particular model tested, which is similar to the preferred model, this contribution is not enough to reproduce the observed lightcurves. However, due to clumping or asymmetries, low density components may exists in the ejecta, for which freeze-out would occur earlier. The 678 day spectrum of SN 2011dh presented by Shivvers et al. (2013), shows features not present in our last optical spectra that *could* be identified as the He I 6678 Å and 7065 Å lines, whereas the strong feature identified as Na I 5890,5896 Å by the authors *could* have a significant contribution from, or be fed by, the He I 5876 Å line. This is consistent with a contribution from recombination emission due to freeze-out in the helium envelope.

CSM interaction became the dominant energy source at ~300 days for SN 1993J, giving rise to broad box-like Hα and Na I 5890,5896 Å lines and a considerable flattening of the lightcurves. The 678 day spectrum of SN 2011dh shows a feature that Shivvers et al. (2013) interpret as broad box-like Hα emission, but no broad box-like Na I 5890,5896 Å emission is seen. The interpretation of the broad feature as Hα emission is far from clear, as a number of other lines may contribute in this wavelength range (including the [N II] 6548,6583 Å line discussed in Sect. 3.2 and the He I 6678 Å line mentioned above), and the feature is much weaker than for SN 1993J at a similar epoch. Additional energy could also be provided by the decay of radioactive isotopes other than ^{56}Co. In the preferred steady-state NLTE model, the fractional bolometric luminosity deposited by the ^{57}Co decay is ~10 percent at 700 days and increasing. A higher mass of ^{57}Co would help explain the observed evolution and can not be excluded. A thermal echo from heated CSM dust could possibly power the MIR pseudo-bolometric lightcurve, but can not explain the behaviour of the optical pseudo-bolometric lightcurve. Another possibility is that the observed flux does not solely originates from the SN, but this seems to be ruled out by the 678 day spectrum, which is line dominated and have a minimum flux level close to zero. In summary we find observational and theoretical evidence that the contribution from the positrons emitted in the ^{56}Co decay does not dominate the observed $\gtrsim$600 days luminosity. A substantial contribution from time-dependent effects is likely, whereas contributions from other energy sources can not be excluded.

6. Conclusions

We present the post 100 days part of our optical and NIR, photometric and spectroscopic dataset for the Type IIb SN 2011dh. The dataset spans two years, and together with SWIFT and Spitzer observations it covers the UV to MIR wavelength range, although the photometric coverage ends at ~100 days in UV and at ~400 days in NIR, and the spectral coverage ends at ~200 days in NIR and at ~450 days in the optical. Particular attention is paid to the bolometric and broad-band lightcurves, where we use steady-state NLTE modelling and hydrodynamical modelling to put constraints on the SN and progenitor parameters. We also provide a spectral analysis, mainly related to the line profiles, complementary to the steady-state NLTE modelling of nebular spectra presented in J14.

We analyse the <400 days optical to MIR pseudo-bolometric lightcurve of SN 2011dh, using a grid of hydrodynamical SN models calculated with HYDE, and a UV to MIR BC determined with steady-state NLTE modelling. This method allows us to determine the errors in the model parameters arising from the uncertainties in the observed quantities, and the degeneracy of the solution. Using this method we find model parameters consistent within error bars with those obtained in B12 using the <80 days UV to MIR pseudo-bolometric lightcurve. In particular we find a helium core mass of $3.1^{+0.7}_{-0.4}$ M$_\odot$ which, taking into account also the degeneracy of the solution, gives upper limits on the helium core and initial mass of $\lesssim$4 M$_\odot$ and $\lesssim$15 M$_\odot$, respectively.

We analyse the 100−500 days pseudo-bolometric and broad-band lightcurves of SN 2011dh, using the set of steady-state NLTE models presented in J14. To extend the temporal coverage of these models, we construct <100 days bolometric lightcurves using HYDE. The preferred 12 M$_\odot$ (initial mass) model, presented in J14, refined in this work with respect to the dust, and chosen to give the best agreement with both spectra and lightcurves, shows an overall agreement with the observed broad-band and pseudo-bolometric lightcurves. In particular, the simultaneous increase in the optical pseudo-bolometric decline rate and the fractional K and S_1 luminosities between 100 and 250 days is reproduced by this model, which has a modest dust opacity in the core ($\tau_{\rm dust} = 0.44$), turned on at 200 days. A local origin of the excess emission is supported by the depth of the He I 20581 Å absorption. We find the dust contribution insufficient to reproduce the S_2 magnitudes and, assuming this additional excess to be dominated by CO fundamental band emission, an intermediate amount of CO cooling in O/C zone is likely. This is consistent with the detected CO first overtone emission, although the fundamental to first overtone band ratios needs to be significantly higher than observed in SN 1987A.

The >500 days lightcurves can not be analysed with the steady-state NLTE code, as the steady-state assumption is no longer valid, but there is both observational and theoretical evidence that the SN becomes powered by additional energy sources in this phase. At >400 days the optical and MIR pseudo-bolometric lightcurves flattens to fast, and at >600 days their luminosities becomes too high, to be powered by the radioactive energy deposition. Modelling with a time-dependent NLTE code (Kozma & Fransson 1992, 1998a,b) shows that time-dependent effects become important at ~600 days, and after ~800 days they provide a dominant and increasing contribution to the optical luminosity. We find substantial contributions from CSM interaction and other radioactive isotopes less likely, whereas a substantial contribution from coincident sources is ruled out.

We estimate progressively smaller sizes, ranging from ~3000 to ~1500 km s^{-1}, for the line emitting regions of oxygen, magnesium, [Ca II] 7291,7323 Å and iron. Given the findings in J14, these regions correspond to the oxygen, O/Ne/Mg, Si/S and Fe/Co/He nuclear burning zones, and suggest incomplete mix-

ing of the core material. The profiles of the [O I] 6300 Å and Mg I] 4571 Å lines show a remarkable similarity, suggesting these lines to arise from the O/Ne/Mg zone. We use repetitions of small scale fluctuations in the [O I] 6300 Å and [O I] 6364 Å lines to find a line ratio close to 3, consistent with optically thin emission, from 200 days and onwards. Applying the method of Chugai (1994) to these small scale fluctuations, we find an upper limit on the filling factor of the [O I] 6300 Å and Mg I] 4571 Å line emitting material of ∼0.07, and a lower limit on the number of clumps of ∼900.

This paper concludes our observational and modelling work on SN 2011dh presented in M11, E14a and J14. Further modelling of our data have been presented by B12. We have applied stellar evolutionary progenitor analysis, hydrodynamical modelling, SN atmosphere modelling and steady-state NLTE modelling to our extensive set of observational data. Although a number of issues remains unsolved, the main characteristics of the SN and its progenitor star found by the different methods are consistent. The progenitor star appears to have been of moderate ($\lesssim$15 $M_\odot$) initial mass, and the 3−4 $M_\odot$ helium core surrounded by a low-mass (∼0.1 $M_\odot$) and extended (200−300 $R_\odot$) hydrogen envelope. Given the upper bound on the initial mass of ∼15 $M_\odot$, the mass-loss rate is probably not strong enough to expel the hydrogen envelope before core-collapse, and a binary origin for SN 2011dh is suggested. Folatelli et al. (2014) find a blue source they suggest to be the companion star in HST UV imaging obtained at ∼1200 days, whereas Maund et al. (2014) find these observations, complemented with optical HST imaging, to be consistent with such a star, but not conclusive, as the SN contribution can not be well constrained. Further observations are likely needed to settle this issue.

7. Acknowledgements

This work is based on observations obtained with the Nordic Optical Telescope, operated by the Nordic Optical Telescope Scientific Association at the Observatorio del Roque de los Muchachos, La Palma, Spain, of the Instituto de Astrofisica de Canarias; the German-Spanish Astronomical Center, Calar Alto, jointly operated by the Max-Planck-Institut für Astronomie Heidelberg and the Instituto de Astrofísica de Andalucía (CSIC); the United Kingdom Infrared Telescope, operated by the Joint Astronomy Centre on behalf of the Science and Technology Facilities Council of the U.K.; the William Herschel Telescope and its service programme (proposals SW2011b21 and SW2012a02), operated on the island of La Palma by the Isaac Newton Group in the Spanish Observatorio del Roque de los Muchachos of the Instituto de Astrofisica de Canarias; the Copernico 1.82m Telescope and Schmidt 67/92 Telescope operated by INAF - Osservatorio Astronomico di Padova at Asiago, Italy; by the 3.6m Italian Telescopio Nazionale Galileo operated by the Fundación Galileo Galilei - INAF on the island of La Palma; the Liverpool Telescope, operated on the island of La Palma by Liverpool John Moores University in the Spanish Observatorio del Roque de los Muchachos of the Instituto de Astrofisica de Canarias with financial support from the UK Science and Technology Facilities Council; the AlbaNova telescope operated by the Department of Astronomy at Stockholm University and funded by a grant from the Knut and Alice Wallenberg Foundation. We acknowledge the exceptional support we got from the NOT staff throughout this campaign, we thank the Calar Alto Observatory for allocation of director's discretionary time and we thank Philip Dufton, Paul Dunstall, Darryl Wright and Lindsay Magill for assistance with the WHT observations.

The Oskar Klein Centre is funded by the Swedish Research Council. J.S. acknowledge support by the Swedish Research Council. S.J.S. thanks European Research Council under the European Union's Seventh Framework Programme (FP7/2007-2013)/ERC Grant agreement n^o [291222] and STFC. A.P., L.T. and S.B. are partially supported by the PRIN-INAF 2011 with the project "Transient Universe: from ESO Large to PESSTO". M.F. acknowledges support by the European Union FP7 programme through ERC grant number 320360. N.E.R. acknowledges the support from the European Union Seventh Framework Programme (FP7/2007-2013) under grant agreement n^o 267251 "Astronomy Fellowships in Italy" (AstroFIt). R.K. acknowledges observing time at the LT, NOT, TNG, and WHT via programme CCI-04. M.M.K. acknowledges generous support from the Hubble Fellowship and Carnegie-Princeton Fellowship.

We thank Melina Bersten for providing the post-explosion density profile for the He4R270 model (B12), for inspiration and a great contribution to the understanding of SN 2011dh. We thank Peter Meikle and Dan Milisavljevic for providing spectra on SN 1993J and SN 2008ax, respectively.

Appendix A: Data reductions and calibration

The reductions and calibration procedures used for the late-time data are the same as described in E14a. Here we discuss data reduction and calibration issues specifically related to the >100 days data.

Appendix A.1: Template subtraction - 100−500 days optical and NIR observations

Comparison of photometry on the original images and on template subtracted images, shows that the background contamination is negligible before ∼300 days, after which we have used photometry on template subtracted images. The optical templates were constructed by point spread function (PSF) subtraction of the SN from observations acquired after 600 days, and the NIR templates by PSF subtraction of the SN from the 339 days WHT observation, which is of excellent quality. For the last 380 days WHT observation we used PSF photometry.

Appendix A.2: S-corrections - 100−500 days optical and NIR observations

The accuracy of the late-time photometry depends critically on the accuracy of the S-corrections. Figure A.1 shows the difference between colour and S-corrections for the Johnson-Cousins (JC) and 2 Micron All Sky Survey (2MASS) systems for most telescope/instrument combinations used. It is clear from this figure that S-corrections are necessary if good precision in the photometry is needed. For some telescope/instrument/band combinations, as for the CA-2.2m/CAFOS and NOT/ALFOSC *I* band and the CA-3.5m/O2000 *J* band, the differences become as large as 0.3-0.5 mag. In particular, the difference between the NOT/ALFOSC and CA-2.2m/CAFOS *I* band observations are ∼0.8 mag at ∼250 days, mainly due to the strong [Ca II] 7291,7323 Å and Ca II 8498,8542,8662 Å lines. As the spectral NIR coverage ends at ∼200 days, we have assumed that the 2MASS S-corrections do not change during the 200-400 days period. This adds uncertainty to the 2MASS photometry after ∼200 days, but as the 2MASS S-corrections, ex-

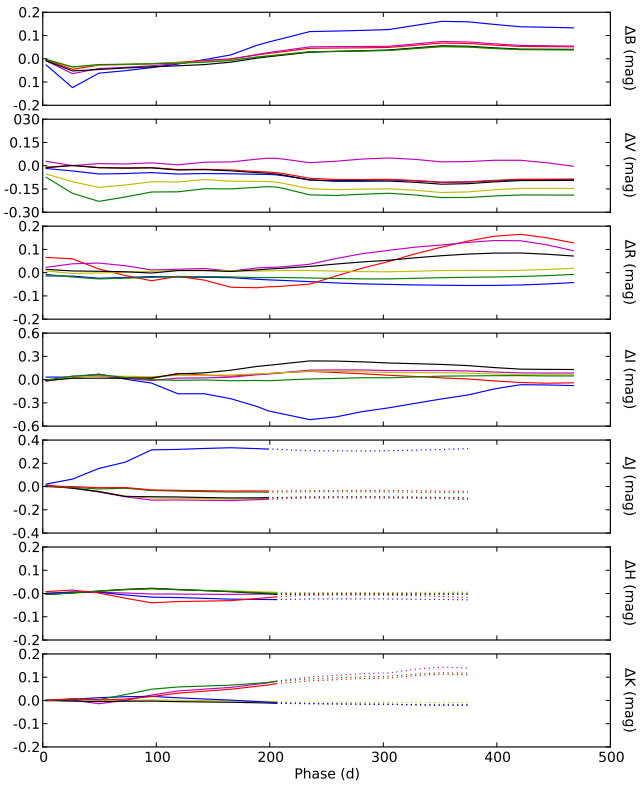

Fig. A.1. Difference between JC *BVRI* colour and S-corrections for NOT/ALFOSC (black), LT/RATCam (red), CA-2.2m/CAFOS (blue), TNG/LRS (green), AS-1.82m/AFOSC (yellow) and AS-Schmidt (magenta), and difference between 2MASS *JHK* colour and S-corrections for NOT/NOTCAM (black), TCS/CAIN (red), CA-3.5m/O2000 (blue), TNG/NICS (green), WHT/LIRIS (yellow) and UKIRT/WFCAM (magenta). Results based on extrapolated 2MASS S-corrections are shown as dotted lines.

cept for the CA-3.5m/O2000 *J* band, are generally small and evolve slowly, the errors arising from this approximation are probably modest. The accuracy of the S-corrections can be estimated by comparing S-corrected photometry obtained with different telescope/instrument combinations. The late-time JC and Sloan Digital Sky Survey (SDSS) photometry were mainly obtained with the NOT, but comparisons between S-corrected NOT/ALFOSC, LT/RATCam and CA-2.2m/CAFOS JC and SDSS observations at ∼300 days, show differences at the 5 percent level, suggesting that the precision from the <100 days period is maintained (E14a). The late-time 2MASS photometry was obtained with a number of different telescopes, and although the sampling is sparse, the shape of the lightcurves suggests that the errors in the S-corrections are modest. Additional filter response functions for AT and UKIRT have been constructed as outlined in E14a.

Appendix A.2.1: Post 600 days optical observations

The results for the post 600 days observations have been adopted from the pre-explosion difference imaging presented in E14a, assuming that the remaining flux at the position of the progenitor originates solely from the SN. The observations were S-corrected using the 678 day spectrum of SN 2011dh presented by Shivvers et al. (2013). Comparing to results from PSF photometry, where we iteratively fitted the PSF subtracted background, we find differences of $\lesssim$0.1 mag. Given that the pre-explosion magnitudes (which were measured with PSF photometry) are correctly measured, the difference based magnitudes are likely to have less uncertainty. On the other hand, the PSF photometry does not depend on the uncertainty in the pre-explosion magnitudes. The good agreement found using these two, partly independent methods gives confidence in the results. Further confidence is gained by comparing the S-corrected NOT and HST (Van Dyk et al. 2013) *V*-band observations, for which we find a difference of $\lesssim$0.2 mag. We are assuming that the flux at the position of the progenitor originates solely from the SN, which should be kept in mind. There is support for this assumption, though, from the depth of absorption features and the line dominated nature of the 678 days spectrum presented by Shivvers et al. (2013).

Appendix A.2.2: Spitzer Telescope observations

For the >100 days photometry we used a small aperture with a 3 pixel radius, and a correction to the standard aperture given in the IRAC Instrument Handbook determined from the images. All images were template subtracted using archival images as described in (E14a). After 100 days, background contamination becomes important, and template subtraction is necessary to obtain precision in the photometry. The <700 days photometry previously published by Helou et al. (2013) agrees very well with our photometry, the differences being mostly $\lesssim$5 percent.

Appendix B: Line measurements

Appendix B.1: Line emitting regions

To estimate the sizes of the line emitting regions, we fit the line profile of a spherically symmetric region of constant line emissivity, optically thin in the line (no line scattering contribution) and with a constant absorptive continuum opacity, to the observed, continuum subtracted (Sect. B.3) line profile. The fitting is done by an automated least-square based algorithm. The absorptive continuum opacity is included to reproduce the blueshifts observed in some line profiles. This method gives a rough estimate of the size of the region responsible for the bulk of the line emission, and is not applied if scattering appears to contribute significantly to the line profile. Some lines arise as a blend of more than one line, which has to be taken into account. The [O I] 6300 Å flux was calculated by iterative subtraction of the [O I] 6364 Å flux, from the left to the right, using $F_{6300}(\lambda) = F_{6300,6364}(\lambda) - F_{6300}(\lambda - \Delta\lambda)/R$, where $\Delta\lambda$ is the wavelength separation between the [O I] 6300 Å and 6364 Å lines and R the [O I] 6300,6364 Å line ratio. This ratio was assumed to be 3, as is supported by the preferred J14 steady-state NLTE model and estimates based on small scale fluctuations in the line profiles (Sect. 3.6). For all other blended lines, we make a simultaneous fit with the line ratios as free parameters, assuming a common size of the line emitting regions.

Appendix B.2: Line asymmetries

To estimate the asymmetry of a line we calculate the first wavelength moment of the flux (center of flux) for the continuum subtracted (Sect. B.3) line profile. The rest wavelength is assumed to be 6316 Å and 7304 Å for the [O I] 6300,6364 Å and [Ca II] 7291,7323 Å lines, respectively, as is appropriate for optically thin emission if we assume the upper levels of the [Ca II]

7291,7323 Å line to be populated as in local thermal equilibrium (LTE). Optically thin emission for these lines is supported by the preferred J14 steady-state NLTE model, the absence of absorption features in the observed spectra and the [O I] 6300,6364 Å line ratio (Sect. 3.6). The rest wavelength is assumed to be 5896 Å and 8662 Å for the Na I 5890,5896 Å and Ca II 8498,8542,8662 Å lines, respectively, as is appropriate for optically thick emission, where emission from the blue lines will eventually scatter in the reddest line. Optically thick emission for the Na I 5896 Å line is supported by the preferred J14 steady-state NLTE model and the observed P-Cygni profile. For the Ca II 8662 Å line this assumption is more doubtful.

Appendix B.3: Continuum subtraction

Before fitting the line emitting region or calculating the center of flux, the (quasi) continuum is subtracted. The continuum level is determined by a linear interpolation between the minimum flux levels on the blue and red sides of the smoothed line profile. The search region is set to ±6000 km s^{-1} for most of the lines, ±10000 km s^{-1} for the Ca II 8662 Å line and ±3000 km s^{-1} for the [Fe II] 7155 Å line.

Appendix B.4: Smalle scale fluctuations

To remove the large scale structure we iteratively (3 times) subtract a 1000 km s^{-1} box average from the line profiles. This method has been tested on the product of synthetic large and small scale structures, and the small scale structures are recovered with reasonable accuracy. Using a Monte-Carlo (MC) analogue of the Chugai (1994) model the (spatial) RMS of the recovered fluctuations is also found to agree well with the actual RMS (δ_F in Chugai 1994, eq. 11)).

Appendix C: Steady-state NLTE modelling.

Appendix C.1: Bolometric corrections

To analyse the effects of the model parameters on the model lightcurves, we make use of a split into a bolometric lightcurve and a bolometric correction (BC). In terms of these quantities, the broad-band magnitudes and the pseudo-bolometric magnitudes (pseudo-bolometric luminosity expressed in bolometric magnitudes) are given by M=M_{Bol}-BC. This split is most useful as the bolometric lightcurve depends only the energy deposition, whereas the BCs depend on how this energy is processed. There is a subtlety here though, as even in steady-state the bolometric luminosity does not equal the energy deposition, because some energy is lost due to scattering in the ejecta. This difference is small (<0.05 mag) and will be ignored in the subsequent discussion. The energy deposition is independent of molecular cooling and dust and, within the parameter space covered by the J14 models, only weakly dependent on the density contrast and the positron trapping. Therefore, the bolometric lightcurves depend significantly only on the initial mass and the macroscopic mixing, whereas the BCs may depend on all model parameters. Figures C.1 and C.2 shows the pseudo-bolometric and broad-band BCs for the J14 models. The optical to MIR BCs show small differences (<±0.1 mag) during the 100−400 days period, but subsequently increase towards ±0.25 mag at 500 days. At 100 days the optical to MIR BC is >−0.15 mag, which is likely to hold at <100 days as well. The optical BCs, on the other hand, show larger differences, mainly because molecular cooling and dust affects the distribution of the flux between the optical and the MIR. Observationally, the split into a bolometric lightcurve and a BC is not straightforward, as we do not know the former and can not calculate the latter. Natural substitutes, which we make use of, are the optical to MIR pseudo-bolometric lightcurve and the quantity $BC_{X,P} = M_{Bol,P} - M_X$, referred to as pseudo-BC, where $M_{Bol,P}$ is the optical to MIR pseudo-bolometric magnitude (see above).

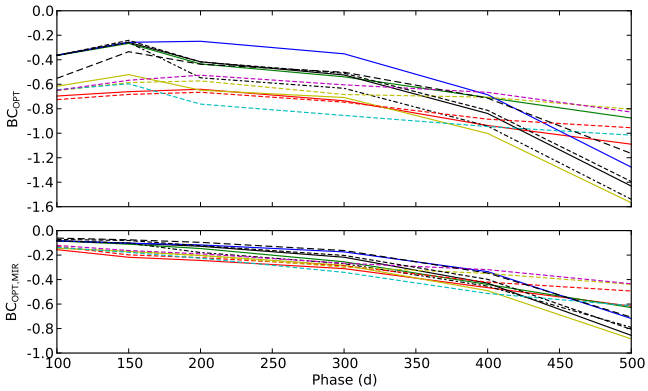

Fig. C.1. 100−500 days optical (upper panel) and optical to MIR (lower panel) BCs for the J14 models. The models are displayed as follows; 12A (red solid line), 12B (green solid line), 12C (black solid line), 12D (yellow solid line), 12E (blue solid line), 12F (black dashed-dotted line), 13A (red short-dashed line), 13C (yellow short-dashed line), 13D (cyan short-dashed line), 13E (magenta short-dashed line), 13G (black short-dashed line), 17A (black long-dashed line).

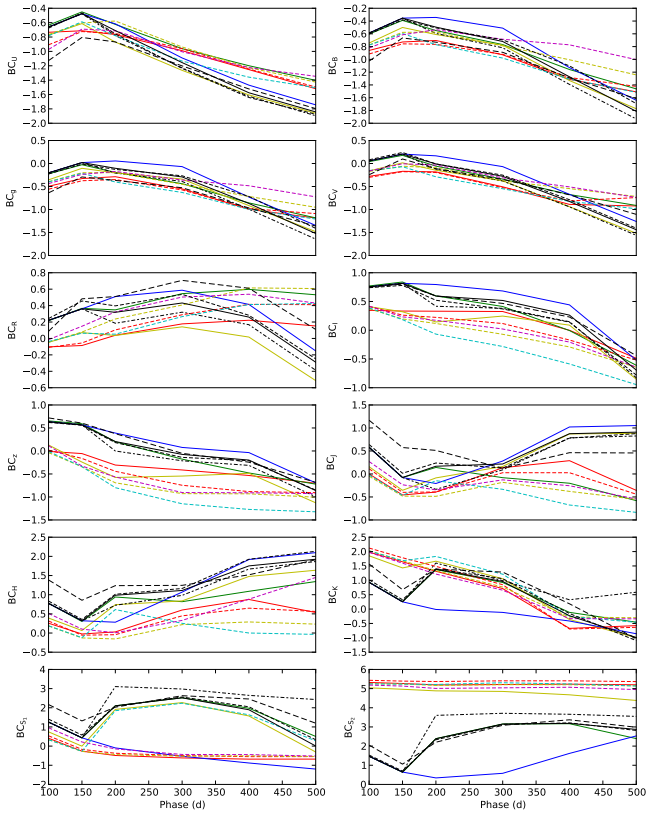

Fig. C.2. 100−500 days broad-band BCs for the J14 models. The models are displayed as in Fig. C.1.

Appendix C.2: Treatment of molecular cooling

Molecular cooling is included in the modelling in a simplified way, and is represented as the fraction of the (radiative and radioactive) heating emitted as molecule (CO and SiO) emission in the O/C and O/Si/S zones. This energy is then emitted as CO and SiO fundamental and first overtone band emission, represented as box line profiles between 2.25−2.45 (CO first overtone), 4.4−4.9 (CO fundamental) and 4.0−4.5 (SiO first overtone) μm. The CO first overtone band overlaps partly with the K band, and the CO fundamental and SiO first overtone bands overlap with the S_2 band, whereas the SiO fundamental band lies outside the U to S_2 wavelength range. The fundamental to first overtone band flux ratios are assumed to be the same as observed for CO in SN 1987A (Bouchet & Danziger 1993). We have used two configurations, one where the fraction of the heating emitted as molecule emission has been set to one, and one where this fraction has been set to zero. Note that CO fundamental band emission dominates the contribution to the S_2 band in all models at all times. This is because the O/Si/S to O/C zone mass ratio and the CO and SiO fundamental to overtone band ratios are all $\lesssim$1, decreasing with increasing initial mass and with time, respectively.

Appendix C.3: Treatment of dust

Dust is included in the modelling in a simplified way, and is represented as a grey absorptive opacity in the core. The absorbed luminosity is re-emitted as blackbody emission with a temperature determined from fits to the photometry. The dust emission is treated separately from the modelling, and is added by post-processing of the model spectra. All the models presented in J14 have the same optical depth and dust temperature, determined from the pseudo-bolometric optical lightcurve and fits to the H, K and S_1 photometry, as described below. In addition we have constructed two new models, 12E which differs from 12C only in the absence of dust and 12F, which differs from 12C only in the optical depth and the method to determine the temperature.

The J14 models have an optical depth of 0.25, turned on at 200 days, which approximately match the behaviour of the optical pseudo-bolometric lightcurve. The temperature is constrained to scale as for a homologously expanding surface, representing a large number of optically thick dust clouds (J14). Minimizing the sum of squares of the relative flux differences of model and observed H, K and S_1 photometry at 200, 300 and 400 days (including H only at 200 days), we find temperatures of 2000, 1097 and 668 K at 200, 300 and 400 days, respectively, given the constraint $T_{dust} < 2000$ K. The S_2 band was excluded as this band might have a contribution from molecule emission, whereas we know that the contribution from CO first overtone emission to the K band at 206 days is negligible. However, the fractional area of the emitting surface (x_{dust}), turns out to be ~20 times smaller than the fractional area needed to reproduce the optical depth, so the derived temperature is not consistent with the assumptions made.

Model 12F has an optical depth of 0.44, turned on at 200 days, which better match the behaviour of the optical pseudo-bolometric lightcurve. The constraint on the temperature evolution used for the J14 models has been abandoned, and fitting the H, K and S_1 photometry as described above, we find temperatures of 1229, 931 and 832 K at 200, 300 and 400 days respectively. This shows that, in addition to the inconsistency between the absorbing and emitting area, the scaling of temperature is not well reproduced by the J14 models. Due to the better reproduction of the optical pseudo-bolometric lightcurve, and the problems with the temperature scaling used for the J14 models, we use model 12F, instead of model 12C, as our preferred model in this paper. Abandoning all attempts to physically explain the temperature, leaves us with black box model, parametrized with the optical depth and the temperature. This is a caveat, but also fair, as the original model with homologously expanding dust clouds, is not self-consistent.

Appendix D: HYDE and the model grid

Here we provide a summary of HYDE and the grid of SN models constructed with this code and MESA STAR (Paxton et al. 2011). A detailed description is provided in E14b, where we also provide tests of HYDE and a detailed analysis of the behaviour of the model grid.

HYDE Is a one-dimensional Lagrangian hydrodynamical code based on the flux limited diffusion approximation, following the method described by Falk & Arnett (1977), and adopting the flux limiter given by Bersten et al. (2011). The opacity is calculated from the OPAL opacity tables (Iglesias & Rogers 1996), complemented with the low temperature opacities given by Alexander & Ferguson (1994). In addition we use an opacity floor set to 0.01 cm^2 gram^{-1} in the hydrogen envelope and 0.025 cm^2 gram^{-1} in the helium core, following Bersten et al. (2012, private communication), who calibrated these values by comparison to the STELLA hydrodynamical code (Blinnikov et al. 1998). The electron density, needed in the equation of state, is calculated by solving the Saha equation using the same atomic data as in Jerkstrand et al. (2011, 2012). The transfer of the gamma-rays and positrons emitted in the decay chain of ^{56}Ni is calculated with a Monte-Carlo method, using the same grey opacities, luminosities and decay times as in Jerkstrand et al. (2011, 2012).

The model grid Is based on non-rotating solar metallicity helium cores, evolved to the verge of core-collapse with MESA STAR (Paxton et al. 2011). The configuration used was the default one, and a central density limit of $10^{9.5}$ gram cm^{-3} was used as termination condition. The evolved models spans M_{He}=4.0−5.0 $M_\odot$ in 0.25 $M_\odot$ steps and M_{He}=5.0−7.0 $M_\odot$ in 0.5 $M_\odot$ steps. Below 4.0 $M_\odot$, stellar models were constructed by a scaling of the 4.0 $M_\odot$ density profile. The SN explosion was parametrized with the injected explosion energy (E), the mass of the ^{56}Ni (M_{Ni}) and the distribution of it. The mass fraction of ^{56}Ni (X_{Ni}) was assumed to be a linearly declining function of the ejecta mass (m_{ej}) becoming zero at some fraction of the total ejecta mass (Mix_{Ni}), expressed as $X_{Ni} \propto 1 - m_{ej}/(Mix_{Ni}M_{ej}), X_{Ni} \geq 0$. Note that this expression allows $Mix_{Ni} > 1$, although the interpretation then becomes less clear. The total volume of parameter space spanned is M_{He}=2.5−7.0 $M_\odot$, E=0.2−2.2×10^{51} erg, M_{Ni}=0.015−0.250 $M_\odot$ and Mix_{Ni}=0.6−1.6 using a 12×16×13×9 grid. A mass cut with zero velocity was set at 1.5 $M_\odot$, the material below assumed to form a compact remnant, although fallback of further material onto this boundary is not prohibited. To calculate 100−400 days bolometric lightcurves we run HYDE in homologous mode, ignore the radiative transfer, and take the bolometric luminosity as the deposited radioactive decay energy (Appendix C.1).

References

Alexander, D. R. & Ferguson, J. W. 1994, ApJ, 437, 879

Arcavi, I., Gal-Yam, A., Yaron, O., et al. 2011, ApJ, 742, L18
Benvenuto, O. G., Bersten, M. C., & Nomoto, K. 2013, ApJ, 762, 74
Bersten, M. C., Benvenuto, O., & Hamuy, M. 2011, ApJ, 729, 61
Bersten, M. C., Benvenuto, O. G., Nomoto, K., et al. 2012, ApJ, 757, 31
Blinnikov, S. I., Eastman, R., Bartunov, O. S., Popolitov, V. A., & Woosley, S. E. 1998, ApJ, 496, 454
Bouchet, P. & Danziger, I. J. 1993, A&A, 273, 451
Chugai, N. N. 1994, ApJ, 428, L17
Ergon, M., Sollerman, J., Fraser, M., et al. 2014a, A&A, 562, A17
Ergon, M., Sollerman, J., Jerkstrand, A., & Fransson, C. 2014b, In preparation
Falk, S. W. & Arnett, W. D. 1977, ApJS, 33, 515
Filippenko, A. V. & Sargent, W. L. W. 1989, ApJ, 345, L43
Folatelli, G., Bersten, M. C., Benvenuto, O. G., et al. 2014, ApJ, 793, L22
Fox, O. D., Azalee Bostroem, K., Van Dyk, S. D., et al. 2014, ArXiv e-prints
Gerardy, C. L., Fesen, R. A., Nomoto, K., et al. 2002, PASJ, 54, 905
Griga, T., Marulla, A., Grenier, A., et al. 2011, Central Bureau Electronic Telegrams, 2736, 1
Helou, G., Kasliwal, M. M., Ofek, E. O., et al. 2013, ApJ, 778, L19
Hunter, D. J., Valenti, S., Kotak, R., et al. 2009, A&A, 508, 371
Iglesias, C. A. & Rogers, F. J. 1996, ApJ, 464, 943
Iwamoto, K., Young, T. R., Nakasato, N., et al. 1997, ApJ, 477, 865
Jerkstrand, A., Ergon, M., Smartt, S., et al. 2014, In preparation
Jerkstrand, A., Fransson, C., & Kozma, C. 2011, A&A, 530, A45
Jerkstrand, A., Fransson, C., Maguire, K., et al. 2012, A&A, 546, A28
Kozma, C. & Fransson, C. 1992, ApJ, 390, 602
Kozma, C. & Fransson, C. 1998a, ApJ, 496, 946
Kozma, C. & Fransson, C. 1998b, ApJ, 497, 431
Lavaux, G. & Hudson, M. J. 2011, MNRAS, 416, 2840
Matheson, T., Filippenko, A. V., Ho, L. C., Barth, A. J., & Leonard, D. C. 2000, AJ, 120, 1499
Matthews, K., Neugebauer, G., Armus, L., & Soifer, B. T. 2002, AJ, 123, 753
Maund, J., Eldridge, J., & Ergon, M. 2014, In preparation
Maund, J. R., Fraser, M., Ergon, M., et al. 2011, ApJ, 739, L37
Maund, J. R., Smartt, S. J., Kudritzki, R. P., Podsiadlowski, P., & Gilmore, G. F. 2004, Nature, 427, 129
Mazzali, P. A., Deng, J., Hamuy, M., & Nomoto, K. 2009, ApJ, 703, 1624
Milisavljevic, D., Fesen, R. A., Gerardy, C. L., Kirshner, R. P., & Challis, P. 2010, ApJ, 709, 1343
Paxton, B., Bildsten, L., Dotter, A., et al. 2011, ApJS, 192, 3
Paxton, B., Cantiello, M., Arras, P., et al. 2013, ApJS, 208, 4
Podsiadlowski, P., Hsu, J. J. L., Joss, P. C., & Ross, R. R. 1993, Nature, 364, 509
Sahu, D. K., Anupama, G. C., & Chakradhari, N. K. 2013, MNRAS, 433, 2
Shetty, R., Vogel, S. N., Ostriker, E. C., & Teuben, P. J. 2007, ApJ, 665, 1138
Shivvers, I., Mazzali, P., Silverman, J. M., et al. 2013, ArXiv e-prints
Spyromilio, J. 1994, MNRAS, 266, L61
Spyromilio, J., Meikle, W. P. S., Learner, R. C. M., & Allen, D. A. 1988, Nature, 334, 327
Stancliffe, R. J. & Eldridge, J. J. 2009, MNRAS, 396, 1699
Stathakis, R. A., Dopita, M. A., Cannon, R. D., & Sadler, E. M. 1991, Supernovae, 649
Suntzeff, N. B. & Bouchet, P. 1990, AJ, 99, 650
Taubenberger, S., Navasardyan, H., Maurer, J. I., et al. 2011, MNRAS, 413, 2140
Tsvetkov, D. Y., Volkov, I. M., Baklanov, P., Blinnikov, S., & Tuchin, O. 2009, Peremennye Zvezdy, 29, 2
Tsvetkov, D. Y., Volkov, I. M., Sorokina, E., et al. 2012, Peremennye Zvezdy, 32, 6
Tully, R. B. 1974, ApJS, 27, 449
Tully, R. B., Shaya, E. J., Karachentsev, I. D., et al. 2008, ApJ, 676, 184
Van Dyk, S. D., Li, W., Cenko, S. B., et al. 2011, ApJ, 741, L28
Van Dyk, S. D., Zheng, W., Clubb, K. I., et al. 2013, ApJ, 772, L32
Woosley, S. E. & Heger, A. 2007, Phys. Rep., 442, 269
Yaron, O. & Gal-Yam, A. 2012, PASP, 124, 668

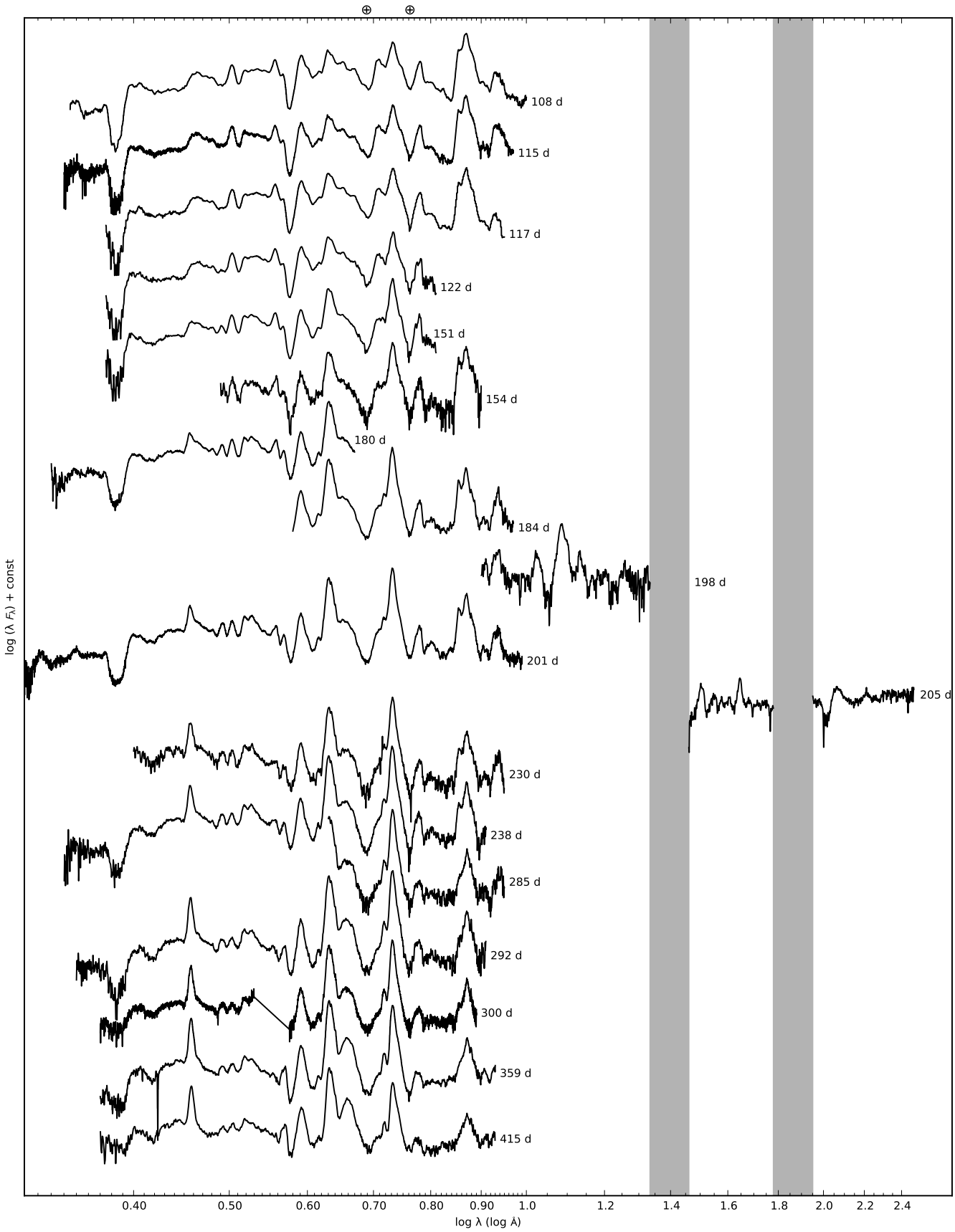

Fig. 7. Sequence of the observed late-time (100−415 days) spectra for SN 2011dh. Spectra obtained on the same night using the same telescope and instrument have been combined and each spectra have been labelled with the phase of the SN. Telluric absorption bands are marked with a ⊕ symbol in the optical and shown as grey regions in the NIR.

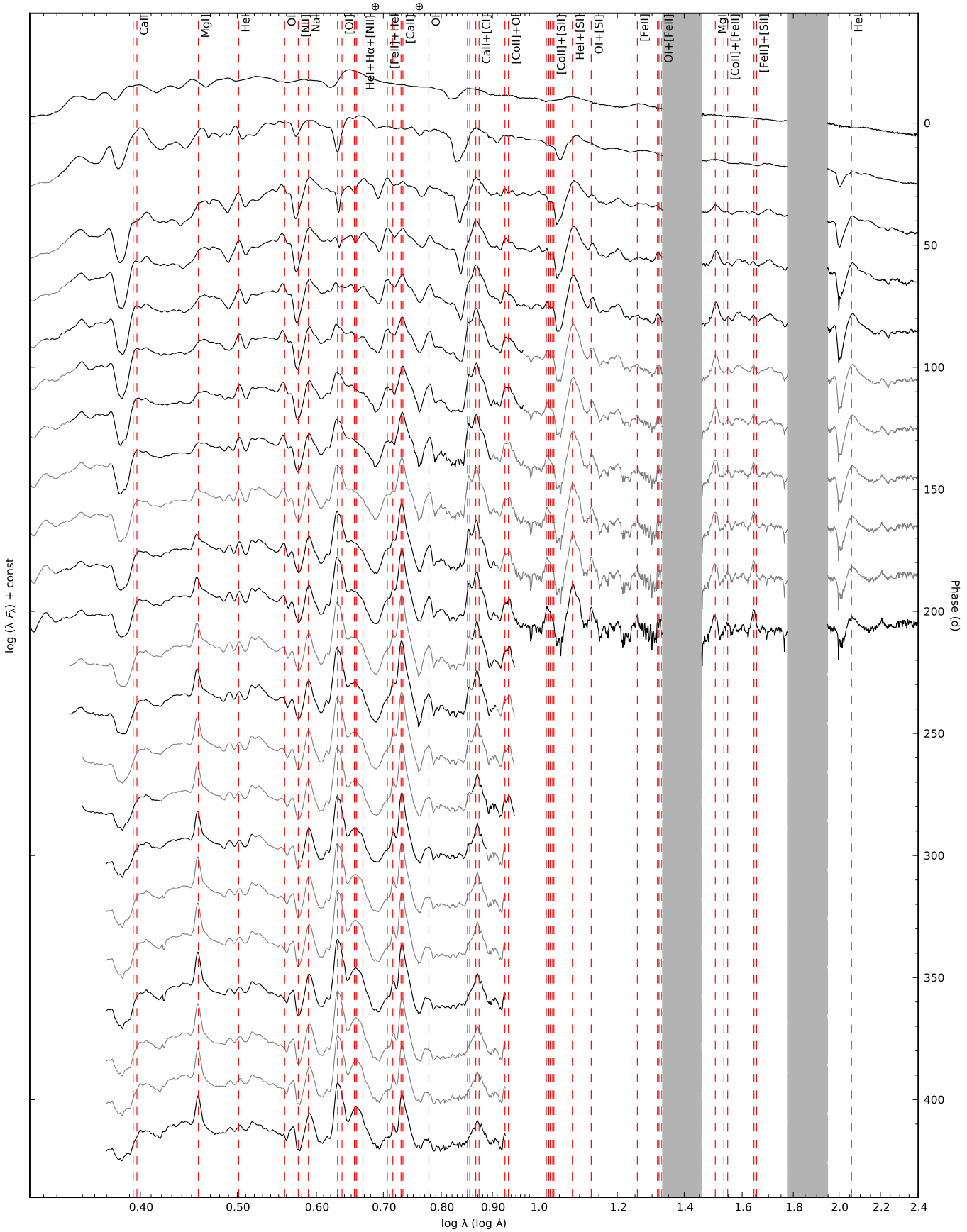

Fig. 8. The 5−425 days optical and NIR (interpolated) spectral evolution for SN 2011dh with a 20-day sampling. Telluric absorption bands are marked with a ⊕ symbol in the optical and shown as grey regions in the NIR.

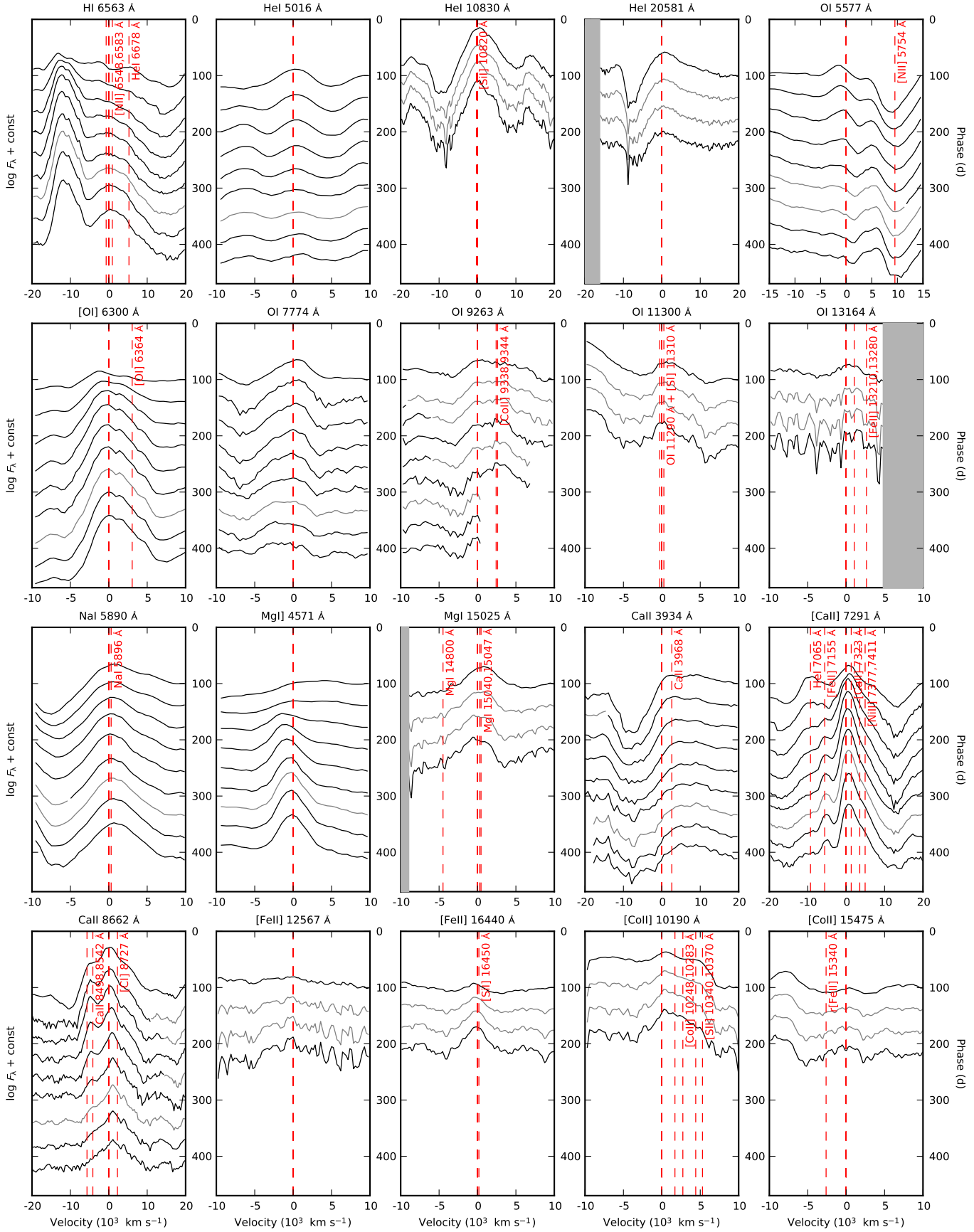

Fig. 9. The >100 days (interpolated) spectral evolution of all identified lines. Multiple or blended lines are marked with red dashed lines and telluric absorption bands in the NIR shown as grey regions.

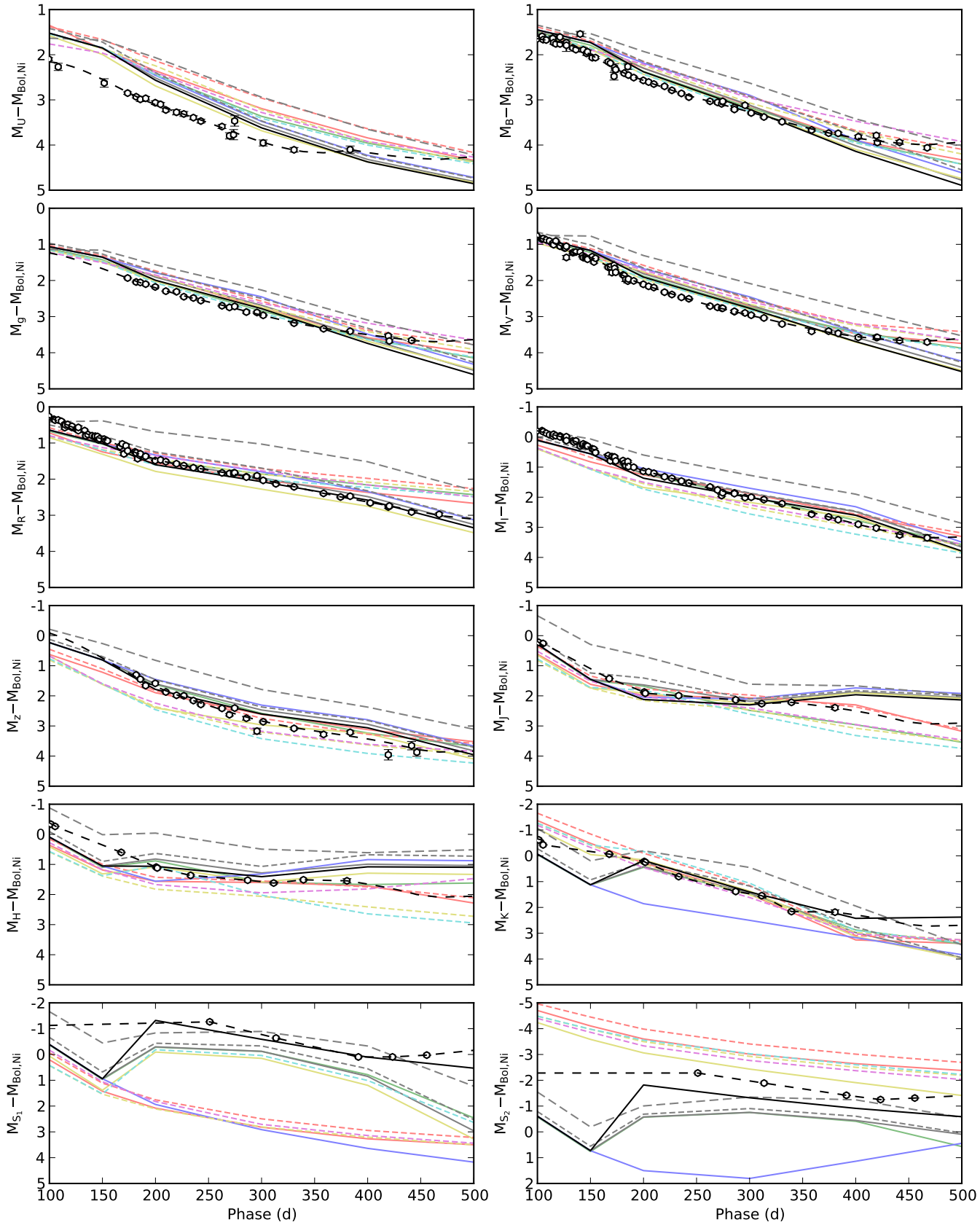

Fig. 17. The 100−500 days observed (black circles) and J14 model optical, NIR and MIR (absolute) magnitudes normalized to the radioactive decay chain luminosity of 0.075 $M_\odot$ of ^{56}Ni. The preferred model (12F) is shown in full colour and all other models in shaded colour. The models are displayed as follows; 12A (red solid line), 12B (green solid line), 12C (black solid line), 12D (yellow solid line), 12E (blue solid line), 12F (black solid line), 13A (red short-dashed line), 13C (yellow short-dashed line), 13D (cyan short-dashed line), 13E (magenta short-dashed line), 13G (black short-dashed line), 17A (black long-dashed line).

Table 4. Late-time (>100 days) optical colour-corrected JC *U* and S-corrected JC *BVRI* magnitudes for SN 2011dh. Errors are given in parentheses.

JD (+2400000) (d)	Phase (d)	*U* (mag)	*B* (mag)	*V* (mag)	*R* (mag)	*I* (mag)	Telescope (Instrument)
55817.35	104.35	...	16.00 0.03	15.20 0.02	14.64 0.02	14.04 0.02	AS-Schmidt (SBIG)
55818.33	105.33	...	16.08 0.02	15.19 0.02	14.68 0.01	14.09 0.01	AS-Schmidt (SBIG)
55821.31	108.31	16.77 0.08	16.12 0.02	15.26 0.01	14.70 0.01	14.17 0.01	CA-2.2m (CAFOS)
55824.32	111.32	...	...	15.31 0.02	14.77 0.03	14.25 0.03	AS-Schmidt (SBIG)
55827.33	114.33	...	16.14 0.03	15.42 0.01	14.88 0.02	14.28 0.01	AS-Schmidt (SBIG)
55827.48	114.48	...	16.15 0.06	15.41 0.03	14.97 0.05	14.32 0.05	AT (ANDOR)
55828.27	115.27	...	16.25 0.03	15.46 0.02	14.91 0.01	14.27 0.01	AT (ANDOR)
55830.28	117.28	...	16.30 0.02	15.38 0.01	14.91 0.01	14.34 0.01	AS-1.82m (AFOSC)
55834.26	121.26	...	16.18 0.03	15.55 0.03	15.03 0.01	14.38 0.02	AT (ANDOR)
55834.31	121.31	...	16.34 0.02	15.56 0.01	15.00 0.02	14.42 0.02	AS-Schmidt (SBIG)
55838.34	125.34	...	...	15.64 0.02	15.12 0.03	14.49 0.01	AS-Schmidt (SBIG)
55839.28	126.28	...	16.37 0.03	15.65 0.02	15.13 0.02	14.52 0.02	AS-Schmidt (SBIG)
55840.26	127.26	...	16.37 0.03	15.62 0.02	15.18 0.02	14.47 0.02	AT (ANDOR)
55840.30	127.30	...	16.42 0.14	15.93 0.06	15.09 0.04	14.60 0.04	AS-Schmidt (SBIG)
55846.26	133.26	...	16.54 0.03	15.85 0.03	15.24 0.02	14.66 0.02	AT (ANDOR)
55847.30	134.30	...	...	15.85 0.03	15.39 0.02	14.71 0.02	AT (ANDOR)
55849.26	136.26	...	16.61 0.04	15.86 0.03	15.38 0.02	14.69 0.02	AT (ANDOR)
55853.27	140.27	...	16.30 0.06	15.90 0.05	15.45 0.05	14.91 0.04	AS-Schmidt (SBIG)
55855.38	142.38	...	...	16.02 0.03	15.50 0.03	14.89 0.03	AT (ANDOR)
55856.24	143.24	...	16.68 0.05	16.08 0.03	15.49 0.02	14.86 0.02	AT (ANDOR)
55858.29	145.29	...	...	16.10 0.03	15.52 0.02	14.92 0.03	AT (ANDOR)
55859.23	146.23	...	16.79 0.04	16.14 0.03	15.62 0.03	14.96 0.03	AT (ANDOR)
55860.22	147.22	...	16.76 0.04	16.17 0.04	15.60 0.02	14.97 0.02	AT (ANDOR)
55864.69	151.69	17.55 0.09	16.94 0.02	16.14 0.01	15.65 0.01	15.10 0.01	AS-1.82m (AFOSC)
55866.28	153.28	...	...	16.30 0.03	15.71 0.02	15.14 0.02	AT (ANDOR)
55867.70	154.70	...	16.97 0.02	16.22 0.03	15.73 0.02	15.26 0.02	CA-2.2m (CAFOS)
55879.66	166.66	...	17.17 0.03	16.58 0.02	16.00 0.02	15.48 0.02	AS-Schmidt (SBIG)
55881.74	168.74	...	17.23 0.02	16.59 0.02	15.95 0.01	15.67 0.03	CA-2.2m (CAFOS)
55883.24	170.24	...	...	16.76 0.06	16.24 0.04	15.55 0.03	AT (ANDOR)
55885.21	172.21	...	17.55 0.08	16.58 0.04	16.04 0.04	15.58 0.03	AT (ANDOR)
55885.73	172.73	...	17.36 0.08	16.67 0.02	...	15.59 0.03	AS-1.82m (AFOSC)
55886.75	173.75	17.99 0.03	17.42 0.01	16.79 0.01	16.19 0.01	15.72 0.01	NOT (ALFOSC)
55893.71	180.71	...	...	16.93 0.02	16.29 0.01	15.78 0.02	AS-Schmidt (SBIG)
55894.76	181.76	18.15 0.02	17.57 0.01	16.96 0.01	16.33 0.01	15.88 0.01	NOT (ALFOSC)
55896.20	183.20	...	...	17.08 0.06	16.50 0.05	15.97 0.04	AT (ANDOR)
55898.19	185.19	...	17.46 0.06	17.14 0.05	16.43 0.04	15.86 0.03	AT (ANDOR)
55898.73	185.73	18.24 0.05	17.65 0.01	17.09 0.01	16.39 0.01	16.03 0.01	NOT (ALFOSC)
55903.76	190.76	18.27 0.04	17.76 0.02	17.19 0.02	16.51 0.02	16.10 0.02	NOT (ALFOSC)
55912.79	199.79	18.46 0.04	17.91 0.02	17.37 0.02	16.72 0.01	16.32 0.01	NOT (ALFOSC)
55917.79	204.79	18.54 0.04	17.99 0.01	17.48 0.01	16.75 0.01	16.39 0.01	NOT (ALFOSC)
55922.76	209.76	18.71 0.04	18.09 0.01	17.56 0.01	16.84 0.01	16.48 0.01	NOT (ALFOSC)
55932.79	219.79	18.86 0.06	18.23 0.01	17.79 0.02	17.00 0.02	16.70 0.02	NOT (ALFOSC)
55939.73	226.73	18.97 0.05	18.39 0.01	17.92 0.02	17.12 0.01	16.82 0.01	NOT (ALFOSC)
55948.73	235.73	19.14 0.04	18.55 0.01	18.09 0.02	17.26 0.01	17.00 0.01	NOT (ALFOSC)
55955.76	242.76	19.28 0.04	18.70 0.01	18.19 0.01	17.36 0.01	17.13 0.01	NOT (ALFOSC)
55975.69	262.69	19.60 0.05	18.98 0.01	18.59 0.01	17.67 0.01	17.45 0.01	NOT (ALFOSC)
55982.74	269.74	19.87 0.07	19.08 0.02	18.69 0.02	17.75 0.01	17.62 0.01	NOT (ALFOSC)
55986.62	273.62	19.88 0.11	19.15 0.03	18.75 0.03	17.78 0.02	17.85 0.03	CA-2.2m (CAFOS)
55987.62	274.62	19.59 0.12	19.10 0.02	18.77 0.02	17.78 0.01	17.76 0.01	LT (RATCam)
55998.66	285.66	...	19.34 0.04	18.97 0.04	18.00 0.02	17.88 0.02	LT (RATCam)
55998.67	285.67	...	19.39 0.02	18.96 0.02	18.01 0.01	17.90 0.01	NOT (ALFOSC)
56008.66	295.66	...	19.39 0.03	19.10 0.03	18.07 0.02	18.13 0.03	LT (RATCam)

Table 5. Continued.

JD (+2400000) (d)	Phase (d)	U (mag)	B (mag)	V (mag)	R (mag)	I (mag)	Telescope (Instrument)
56014.51	301.51	20.34 0.07	19.62 0.01	19.22 0.02	18.25 0.01	18.17 0.01	NOT (ALFOSC)
56026.49	313.49	...	19.83 0.02	19.41 0.02	18.47 0.01	18.37 0.02	NOT (ALFOSC)
56043.59	330.59	20.77 0.05	20.10 0.02	19.75 0.02	18.72 0.01	18.67 0.02	NOT (ALFOSC)
56071.42	358.42	...	20.55 0.02	20.22 0.03	19.17 0.02	19.29 0.03	NOT (ALFOSC)
56087.43	374.43	...	20.78 0.02	20.37 0.03	19.42 0.02	19.54 0.02	NOT (ALFOSC)
56096.48	383.48	21.28 0.08	20.87 0.03	20.52 0.03	19.49 0.02	19.72 0.03	NOT (ALFOSC)
56115.44	402.44	...	21.13 0.03	20.82 0.04	19.86 0.02	20.06 0.04	NOT (ALFOSC)
56132.43	419.43	...	21.27 0.05	20.99 0.05	20.14 0.03	20.35 0.05	NOT (ALFOSC)
56133.40	420.40	...	21.43 0.05	20.99 0.05	20.12 0.03	...	NOT (ALFOSC)
56154.39	441.39	...	21.63 0.04	21.28 0.05	20.49 0.03	20.79 0.06	NOT (ALFOSC)
56180.37	467.37	...	22.01 0.04	21.58 0.05	20.81 0.03	21.14 0.11	NOT (ALFOSC)
56313.73	600.73	...	...	22.44 0.10	...	...	NOT (ALFOSC)
56353.50	640.50	...	...	23.02 0.00	...	22.58 0.00	HST (ACS)
56371.69	658.69	...	23.42 0.32	...	...	...	NOT (ALFOSC)
56397.64	684.64	...	...	23.20 0.20	...	...	NOT (ALFOSC)
56445.43	732.43	...	23.96 0.50	...	...	...	NOT (ALFOSC)

Table 6. Late-time (>100 days) optical colour-corrected SDSS u and S-corrected SDSS $griz$ magnitudes for SN 2011dh. Errors are given in parentheses.

JD (+2400000) (d)	Phase (d)	u (mag)	g (mag)	r (mag)	i (mag)	z (mag)	Telescope (Instrument)
55886.75	173.75	18.76 0.04	16.99 0.01	16.37 0.01	16.14 0.01	...	NOT (ALFOSC)
55894.76	181.76	18.92 0.03	17.18 0.02	16.51 0.01	16.27 0.01	16.29 0.02	NOT (ALFOSC)
55898.73	185.73	19.02 0.04	17.23 0.01	16.58 0.01	16.39 0.01	16.47 0.02	NOT (ALFOSC)
55903.76	190.76	19.13 0.08	17.33 0.02	16.70 0.01	16.45 0.01	16.73 0.04	NOT (ALFOSC)
55912.79	199.79	19.29 0.06	17.49 0.02	16.90 0.01	16.64 0.01	16.74 0.04	NOT (ALFOSC)
55922.77	209.77	19.47 0.02	17.71 0.01	17.03 0.01	16.79 0.01	17.13 0.01	NOT (ALFOSC)
55932.79	219.79	19.62 0.05	17.82 0.02	17.20 0.02	16.96 0.02	17.33 0.04	NOT (ALFOSC)
55939.74	226.74	19.76 0.05	18.03 0.01	17.31 0.01	17.07 0.01	17.42 0.02	NOT (ALFOSC)
55948.73	235.73	19.93 0.03	18.15 0.01	17.45 0.01	17.22 0.01	17.67 0.01	NOT (ALFOSC)
55955.76	242.76	20.08 0.03	18.29 0.01	17.56 0.01	17.34 0.01	17.86 0.02	NOT (ALFOSC)
55975.69	262.69	20.32 0.04	18.63 0.01	17.84 0.01	17.65 0.01	18.19 0.02	NOT (ALFOSC)
55982.74	269.74	20.68 0.06	18.74 0.01	17.94 0.01	17.83 0.01	18.47 0.03	NOT (ALFOSC)
55987.62	274.62	20.49 0.11	18.76 0.01	17.95 0.01	17.94 0.01	18.29 0.03	LT (RATCam)
55998.66	285.66	...	19.02 0.03	18.15 0.02	18.06 0.02	18.74 0.06	LT (RATCam)
56008.66	295.66	...	19.13 0.02	18.22 0.01	18.31 0.03	19.26 0.10	LT (RATCam)
56014.52	301.52	21.08 0.05	19.27 0.01	18.39 0.01	18.41 0.01	19.01 0.02	NOT (ALFOSC)
56043.60	330.60	21.53 0.04	19.77 0.01	18.81 0.01	18.91 0.01	19.51 0.03	NOT (ALFOSC)
56071.43	358.43	...	20.20 0.02	19.23 0.02	19.56 0.03	19.98 0.05	NOT (ALFOSC)
56096.49	383.49	22.07 0.07	20.51 0.02	19.52 0.02	20.00 0.03	20.16 0.05	NOT (ALFOSC)
56132.43	419.43	...	20.99 0.03	20.16 0.02	20.65 0.04	21.25 0.17	NOT (ALFOSC)
56133.41	420.41	...	21.14 0.04	20.13 0.03	20.78 0.05	...	NOT (ALFOSC)
56154.39	441.39	...	21.32 0.04	20.51 0.03	21.10 0.06	21.17 0.14	NOT (ALFOSC)
56159.38	446.38	...	...	...	...	21.43 0.13	NOT (ALFOSC)
56313.75	600.75	...	...	22.46 0.11	...	...	NOT (ALFOSC)
56428.46	715.46	...	...	23.10 0.20	...	...	NOT (ALFOSC)

Table 7. Late-time (>100 days) NIR S-corrected 2MASS JHK magnitudes for SN 2011dh. Errors are given in parentheses.

JD (+2400000) (d)	Phase (d)	J (mag)	H (mag)	K (mag)	Telescope (Instrument)
55814.32	101.32	14.38 0.01	13.80 0.01	13.50 0.01	CA-3.5m (O2000)
55818.36	105.36	14.45 0.02	13.91 0.01	13.74 0.01	NOT (NOTCAM)
55880.72	167.72	16.23 0.01	15.38 0.01	14.70 0.01	CA-3.5m (O2000)
55913.68	200.68	17.00 0.01	16.19 0.02	15.31 0.02	CA-3.5m (O2000)
55914.66	201.66	17.05 0.01	16.23 0.02	15.35 0.02	CA-3.5m (O2000)
55946.13	233.13	17.43 0.02	16.78 0.02	16.21 0.02	UKIRT (WFCAM)
55999.91	286.91	18.10 0.02	17.47 0.02	17.31 0.02	UKIRT (WFCAM)
56024.38	311.38	18.46 0.03	17.80 0.03	17.71 0.04	WHT (LIRIS)
56052.47	339.47	18.69 0.02	17.96 0.02	18.60 0.03	WHT (LIRIS)
56093.48	380.48	19.27 0.06	18.40 0.07	19.02 0.09	WHT (LIRIS)

Table 8. MIR Spitzer S_1 and S_2 magnitudes for SN 2011dh. Errors are given in parentheses.

JD (+2400000) (d)	Phase (d)	S_1 (mag)	S_2 (mag)	Telescope (Instrument)
55964.14	251.14	14.300 0.002	13.280 0.002	SPITZER (IRAC)
56026.63	313.63	15.536 0.007	14.280 0.003	SPITZER (IRAC)
56104.23	391.23	17.025 0.012	15.507 0.005	SPITZER (IRAC)
56136.41	423.41	17.337 0.014	15.988 0.006	SPITZER (IRAC)
56168.69	455.69	17.581 0.014	16.241 0.008	SPITZER (IRAC)
56337.59	624.59	18.517 0.083	17.537 0.056	SPITZER (IRAC)
56360.27	647.27	18.675 0.045	17.663 0.030	SPITZER (IRAC)
56477.83	764.83	18.833 0.047	18.047 0.039	SPITZER (IRAC)
56742.28	1029.28	...	18.506 0.091	SPITZER (IRAC)
56742.30	1029.30	...	18.410 0.075	SPITZER (IRAC)
56771.67	1058.67	18.858 0.077	18.543 0.070	SPITZER (IRAC)
56773.84	1060.84	...	18.364 0.058	SPITZER (IRAC)

Table 9. List of late-time (100−415 days) optical and NIR spectroscopic observations.

JD (+2400000) (d)	Phase (d)	Grism	Range (Å)	Resolution	Resolution (Å)	Telescope (Instrument)
55821.33	108.33	b200	3300-8700	...	12.0	CA-2.2m (CAFOS)
55821.33	108.33	r200	6300-10500	...	12.0	CA-2.2m (CAFOS)
55828.35	115.35	R300B	3200-5300	...	4.1	WHT (ISIS)
55828.35	115.35	R158R	5300-10000	...	7.7	WHT (ISIS)
55830.25	117.25	Grism 4	3500-8450	292	19.9	AS 1.82m (AFOSC)
55830.28	117.28	Grism 2	3720-10200	191	37.6	AS 1.82m (AFOSC)
55835.25	122.25	Grism 4	3500-8450	292	19.9	AS 1.82m (AFOSC)
55864.65	151.65	Grism 4	3500-8450	292	19.9	AS 1.82m (AFOSC)
55867.71	154.71	g200	4900-9900	...	12.0	CA-2.2m (CAFOS)
55893.76	180.76	Grism 3	3200-6700	345	12.4	NOT (ALFOSC)
55897.76	184.76	Grism 5	5000-10250	415	16.8	NOT (ALFOSC)
55911.20	198.20	zJ	8900-15100	700	...	WHT (LIRIS)
55914.70	201.70	R300B	3200-5300	...	8.2	WHT (ISIS)
55914.70	201.70	R158R	5300-10000	...	15.4	WHT (ISIS)
55918.69	205.69	HK	14000-25000	333	...	TNG (NICS)
55941.72	228.72	R150V	4000-9500	...	12.9	INT (IDS)
55942.73	229.73	R150V	4000-9500	...	12.9	INT (IDS)
55944.75	231.75	R150V	4000-9500	...	12.9	INT (IDS)
55951.64	238.64	Grism 4	3200-9100	355	16.2	NOT (ALFOSC)
55998.68	285.68	r200	6300-10500	...	12.0	CA-2.2m (CAFOS)
56002.58	289.58	Grism 4	3200-9100	355	16.2	NOT (ALFOSC)
56005.62	292.62	Grism 4	3200-9100	355	16.2	NOT (ALFOSC)
56006.60	293.60	Grism 4	3200-9100	355	16.2	NOT (ALFOSC)
56013.14	300.14	R600B	3680-5300	...	5.7	WHT (ISIS)
56013.14	300.14	R316R	5756-8850	...	3.0	WHT (ISIS)
56071.56	358.56	R500B	3440-7600	322	15.0	GTC (OSIRIS)
56072.61	359.61	R500R	4800-10000	352	20.8	GTC (OSIRIS)
56128.47	415.47	R300B	3600-7000	270	16.7	GTC (OSIRIS)

Table 10. Pseudo-bolometric 3−400 days UV to MIR lightcurve for SN 2011dh calculated from spectroscopic and photometric data with a 1-day sampling between 3 and 50 days and a 5-day sampling between 50 and 400 days. Random errors are given in the first parentheses and systematic lower and upper errors (arising from the distance and extinction) respectively in the second parentheses.

JD (+2400000) (d)	Phase (d)	L (log erg s^{-1})	JD (+2400000) (d)	Phase (d)	L (log erg s^{-1})
55717.00	4.00	41.464 (0.001) (0.098,0.186)	55823.00	110.00	41.244 (0.002) (0.094,0.164)
55718.00	5.00	41.552 (0.001) (0.097,0.181)	55828.00	115.00	41.204 (0.002) (0.094,0.164)
55719.00	6.00	41.653 (0.001) (0.097,0.179)	55833.00	120.00	41.163 (0.002) (0.094,0.164)
55720.00	7.00	41.747 (0.001) (0.097,0.178)	55838.00	125.00	41.121 (0.002) (0.094,0.164)
55721.00	8.00	41.835 (0.001) (0.097,0.178)	55843.00	130.00	41.078 (0.002) (0.094,0.164)
55722.00	9.00	41.909 (0.001) (0.097,0.178)	55848.00	135.00	41.033 (0.002) (0.094,0.165)
55723.00	10.00	41.969 (0.001) (0.097,0.177)	55853.00	140.00	40.990 (0.002) (0.094,0.165)
55724.00	11.00	42.018 (0.001) (0.097,0.176)	55858.00	145.00	40.948 (0.002) (0.094,0.165)
55725.00	12.00	42.057 (0.001) (0.097,0.176)	55863.00	150.00	40.906 (0.002) (0.094,0.165)
55726.00	13.00	42.089 (0.001) (0.096,0.175)	55868.00	155.00	40.863 (0.002) (0.094,0.165)
55727.00	14.00	42.117 (0.001) (0.096,0.174)	55873.00	160.00	40.818 (0.002) (0.094,0.165)
55728.00	15.00	42.142 (0.001) (0.096,0.174)	55878.00	165.00	40.773 (0.002) (0.094,0.164)
55729.00	16.00	42.163 (0.001) (0.096,0.173)	55883.00	170.00	40.728 (0.002) (0.094,0.164)
55730.00	17.00	42.182 (0.001) (0.096,0.173)	55888.00	175.00	40.683 (0.002) (0.094,0.164)
55731.00	18.00	42.197 (0.001) (0.096,0.173)	55893.00	180.00	40.639 (0.001) (0.094,0.164)
55732.00	19.00	42.208 (0.001) (0.096,0.172)	55898.00	185.00	40.597 (0.001) (0.094,0.164)
55733.00	20.00	42.214 (0.001) (0.096,0.172)	55903.00	190.00	40.555 (0.001) (0.094,0.164)
55734.00	21.00	42.215 (0.001) (0.096,0.171)	55908.00	195.00	40.516 (0.001) (0.094,0.164)
55735.00	22.00	42.211 (0.001) (0.095,0.171)	55913.00	200.00	40.477 (0.001) (0.094,0.164)
55736.00	23.00	42.200 (0.001) (0.095,0.170)	55918.00	205.00	40.438 (0.001) (0.094,0.164)
55737.00	24.00	42.184 (0.001) (0.095,0.168)	55923.00	210.00	40.403 (0.001) (0.094,0.164)
55738.00	25.00	42.164 (0.001) (0.095,0.167)	55928.00	215.00	40.368 (0.001) (0.094,0.164)
55739.00	26.00	42.141 (0.001) (0.094,0.166)	55933.00	220.00	40.334 (0.001) (0.094,0.164)
55740.00	27.00	42.116 (0.001) (0.094,0.165)	55938.00	225.00	40.300 (0.001) (0.094,0.164)
55741.00	28.00	42.090 (0.001) (0.094,0.164)	55943.00	230.00	40.267 (0.001) (0.094,0.164)
55742.00	29.00	42.064 (0.001) (0.094,0.163)	55948.00	235.00	40.235 (0.001) (0.094,0.163)
55743.00	30.00	42.039 (0.001) (0.094,0.162)	55953.00	240.00	40.204 (0.001) (0.094,0.163)
55744.00	31.00	42.016 (0.001) (0.093,0.162)	55958.00	245.00	40.172 (0.001) (0.094,0.163)
55745.00	32.00	41.995 (0.001) (0.093,0.161)	55963.00	250.00	40.139 (0.001) (0.094,0.163)
55746.00	33.00	41.976 (0.001) (0.093,0.161)	55968.00	255.00	40.106 (0.001) (0.094,0.163)
55747.00	34.00	41.959 (0.001) (0.093,0.160)	55973.00	260.00	40.072 (0.001) (0.094,0.163)
55748.00	35.00	41.942 (0.001) (0.093,0.160)	55978.00	265.00	40.039 (0.002) (0.094,0.163)
55749.00	36.00	41.927 (0.001) (0.093,0.160)	55983.00	270.00	40.005 (0.002) (0.094,0.163)
55750.00	37.00	41.913 (0.001) (0.093,0.159)	55988.00	275.00	39.972 (0.002) (0.094,0.163)
55751.00	38.00	41.899 (0.001) (0.093,0.159)	55993.00	280.00	39.939 (0.002) (0.094,0.163)
55752.00	39.00	41.885 (0.001) (0.093,0.159)	55998.00	285.00	39.906 (0.002) (0.094,0.163)
55753.00	40.00	41.873 (0.001) (0.093,0.159)	56003.00	290.00	39.872 (0.002) (0.094,0.163)
55754.00	41.00	41.859 (0.001) (0.093,0.159)	56008.00	295.00	39.838 (0.002) (0.094,0.163)
55755.00	42.00	41.846 (0.001) (0.093,0.159)	56013.00	300.00	39.804 (0.002) (0.094,0.163)
55756.00	43.00	41.834 (0.001) (0.093,0.159)	56018.00	305.00	39.770 (0.002) (0.094,0.163)
55757.00	44.00	41.822 (0.002) (0.093,0.159)	56023.00	310.00	39.737 (0.002) (0.094,0.163)
55758.00	45.00	41.811 (0.002) (0.093,0.159)	56028.00	315.00	39.703 (0.002) (0.094,0.163)
55759.00	46.00	41.800 (0.001) (0.093,0.159)	56033.00	320.00	39.670 (0.002) (0.094,0.163)
55760.00	47.00	41.790 (0.001) (0.093,0.159)	56038.00	325.00	39.638 (0.002) (0.094,0.163)
55761.00	48.00	41.781 (0.001) (0.093,0.159)	56043.00	330.00	39.605 (0.002) (0.094,0.163)
55762.00	49.00	41.771 (0.002) (0.093,0.159)	56048.00	335.00	39.572 (0.002) (0.094,0.163)
55763.00	50.00	41.762 (0.002) (0.093,0.159)	56053.00	340.00	39.540 (0.002) (0.094,0.163)
55768.00	55.00	41.715 (0.002) (0.093,0.159)	56058.00	345.00	39.508 (0.002) (0.094,0.163)
55773.00	60.00	41.669 (0.002) (0.093,0.159)	56063.00	350.00	39.476 (0.002) (0.094,0.163)
55778.00	65.00	41.627 (0.002) (0.093,0.160)	56068.00	355.00	39.445 (0.002) (0.094,0.163)
55783.00	70.00	41.585 (0.002) (0.093,0.160)	56073.00	360.00	39.413 (0.002) (0.094,0.163)
55788.00	75.00	41.544 (0.002) (0.093,0.161)	56078.00	365.00	39.382 (0.002) (0.094,0.163)
55793.00	80.00	41.501 (0.002) (0.093,0.162)	56083.00	370.00	39.351 (0.002) (0.094,0.163)
55798.00	85.00	41.458 (0.002) (0.094,0.162)	56088.00	375.00	39.320 (0.002) (0.094,0.163)
55803.00	90.00	41.415 (0.002) (0.094,0.162)	56093.00	380.00	39.289 (0.002) (0.094,0.163)
55808.00	95.00	41.372 (0.002) (0.094,0.163)	56098.00	385.00	39.255 (0.002) (0.094,0.163)
55813.00	100.00	41.330 (0.002) (0.094,0.163)	56103.00	390.00	39.220 (0.002) (0.094,0.163)
55818.00	105.00	41.287 (0.002) (0.094,0.163)	56108.00	395.00	39.186 (0.002) (0.094,0.164)